

(NASA-CR-158499) MICROSCOPIC PHENOMENA AND  
A MODERN APPROACH TO TURBULENCE Final  
Report, Jun. 1976: - Jul. 1978 (Rutgers: - The  
State Univ.) 86 p HC A05/MF A01 CSCL 01A

N79-22045

Unclas  
25104

G3/02

## PHYSICS DEPARTMENT



**RUTGERS**  
THE STATE UNIVERSITY  
OF NEW JERSEY



MICROSCOPIC PHENOMENA AND A MODERN  
APPROACH TO TURBULENCE

J. A. Johnson III, S. Chen, L. I,  
W. Jones, R. Ramaiah, J. Santiago

MICROSCOPIC PHENOMENA AND A MODERN  
APPROACH TO TURBULENCE

Joseph A. Johnson III, Shen Chen, Lin I, Walter Jones,  
Raghu Ramaiah, Jaime Santiago

Department of Physics  
Rutgers University, New Brunswick, N. J. 08903

April 2, 1979

## Abstract

This document is a final technical report on a National Aeronautics and Space Administration research grant titled "Three Body Recombination in Supersonic Flow", NSG 1314, June, 1976 through July, 1978, from NASA Langley Research Center. The investigators proposed to look for diagnostic techniques and experimental evidence to support new approaches to the turbulence problem using the shock tube and to undertake related theoretical studies as well. Evidence to support a kinetic theory of turbulence has been found. An overview of these and other achievements to date is given herein.

## Table of Contents

|     |   |    |
|-----|---|----|
| I   | Introduction  | 1  |
| II  | Reaction Rate Distortion in Turbulent Flow                          | 2  |
| III | Turbulent Bursts in a Shock Tube                                    | 8  |
| IV  | Driver Gas Flow with Fluctuations                                   | 14 |
| V   | Improving the Mach Number Capabilities of Arc<br>Driver Shock Tubes | 42 |
| VI  | Resonant Absorption in an Argon Plasma at Thermal<br>Equilibrium    | 55 |
| VII | Summary   | 67 |
|     | References  | 69 |
|     | Appendix A: Bibliography, NSG 1314                                  | 72 |

## Table Captions

|         |   |    |
|---------|---|----|
| Table I | The Performance of Pressure Loaded Arc Driven Shock Tubes. See text for the explanation of symbols. | 54 |
|---------|---|----|

## Figure Captions

- Figure 1      The growth of the turbulent intensity of bursts      13  
in an unstable detonation front. The Reynolds number is based on the displacement thickness as measured from an interferogram of the front from reference 9. The quantity  $(\overline{\Delta S^2})^{1/2}$  is the root mean squared averaged value of the fluctuations about an average fringe shift in the turbulent burst. The quantity  $I$  is defined in the text. The dashed straight line is a fit to the four data points indicated which shows a slope  $(d(\log I)/dRe = 3.2 \times 10^{-3})$  consistent with theoretical expectations.
- Figure 2      Overall Shock Tube Flow. This is an  $(x,t)$       16  
diagram. A partition separates two regions in the shock tube with high pressure gas occupying  $x < 0$  at  $t < 0$  and the gas originally at low pressure occupying  $x > 0$  at  $t < 0$ . Examples of the various discontinuities and wave phenomena in the shock tube subsequent ( $t > 0$ ) to the rupture of the partition at  $x = 0, t = 0$  are shown. (S) is the shock wave; (C) is the contact surface; (T) is the tail of the expansion fan (in this case  $(v_3 - a_3) > 0$ ); (H) is the head of the expansion fan. (See text.)

- Figure 3      The Test Section.      Some of the pressure gauges      19  
are indicated along the top of the tube. The  
optical path through the test section is shown  
in its Michelson-Morley interferometer mode. A  
single fringe from the interferometer is shared  
by two light pipes which provide, with associated  
photo-electronics, signals F1 and F2 respectively.  
The insert shows a sample of calibration data for  
 $F = F1 - F2$  confirming fringe shift cancellation for  
unsteady irregular flow where the correlation  
length scale is large compared to the separation  
between the light pipes.
- Figure 4      Calibration: Shock Front Pressure Ratio.      Here      22  
 $\Delta P = \{(P_2/P_1)_{\text{meas}} - (P_2/P_1)_{\text{cal}}\}$ :  $(P_2/P_1)_{\text{cal}}$  is  
the pressure ratio calculated from the measured  
Mach number of the shock wave ( $S$  in Figure 1),  
 $M_s$ , and  $(P_2/P_1)_{\text{meas}}$  is the pressure ratio across  
the shock wave as measured in the test section.
- Figure 5      Calibration: Contact Surface Time of Flight.      24  
 $T_{c,M}$  is the measured time interval between the  
arrival of the shock wave at  $x = +76.4$  cm in the  
test section and the appearance of rapid irregular  
density fluctuations (i.e., at F1) as indicated  
by one of the light pipes in Figure 2. This is  
schematically indicated in the sketch where P  
shows pressure versus time and the arrival of



the shock wave and D shows the output of the interferometer with the amplitude modulation resulting from fringe shifts. A sample of the data, with phototube output (arbitrary units) versus time (50  $\mu$ sec/div.), is displayed as an insert.  $T_{c,c}$  is the calculated value of the interval, using the shock wave's measured Mach number,  $M_s$ , and assuming ideal gas flow, between the arrival of the shock wave and the arrival of the contact surface at the same location.

Figure 6 Calibration: Lambert-Beer's Law Absorption for  $\text{NO}_2$ . Relative absorption of blue light (4350  $\text{\AA}$ ) for several concentrations of  $\text{NO}_2$  appropriate to our operating conditions is shown. The straight line is a best fit to  $(E/E_0) = 10^a$  where  $a = -(0.208 \pm 0.004) [\text{NO}_2]$ . 25

Figure 7 Examples of Large Fluctuations in Pressure. In each photograph, the scales are: vertically, pressure (.14 atm/div); horizontally, time (.5 msec/div). The middle trace (ignore the uppermost trace) is pressure at  $x = +76.4$  cm and the bottom trace is pressure at  $x = +122.1$  cm, further away from the partition. Each photograph shows one or more large fluctuations at  $x = +76.4$  cm subsequently diminishing in deviation at  $x = +122.1$  cm. (a)  $M_s = 2.2$ ,  $(\text{Re}^t/\text{cm}) = 3.9 \times 10^5$ ; (vii) 27

(b)  $M_s = 2.2$ ,  $(Re^t/cm) = 4.4 \times 10^5$ ; (c)  $M_s = 2.0$ ,  $(Re^t/cm) = 2.7 \times 10^5$ ; (d)  $M_s = 2.0$ ,  $(re^t/cm) = 3.8 \times 10^5$ .

Figure 8      An Example of Total Gas Density Sudden Coherence      28  
 Associated with a Large Pressure Fluctuation. The top trace is the pressure gauge's output. The bottom trace is the (simultaneous) output of  $F (= F_1 - F_2)$  from the interferometer located at the same position in the test section as the pressure gauge. The traces shown are as displayed on an X-Y plotter which records the output of the Biomation 8100 ADC. The arrow indicates the large fluctuation in pressure.

Figure 9      An Example of Reactant Gas Density Distortion      29  
 Associated with a Large Pressure Fluctuation. The top trace is the pressure gauge's output. The bottom trace is the (simultaneous) output from the phototube which monitors the absorption of light at  $4350 \text{ \AA}$  along the optical path through the test section. The decreased  $NO_2$  density shows up as decreased absorption and increased negative signal  $E$  at the phototube. The traces shown are as displayed on a computer reconstruction of the output of our analog to digital converter. The arrows indicate the coincident fluctuations.

during a Large Pressure Fluctuation. A segment by segment quadratic fit to the pressure history  $p(t)$  at the test section's window is made after the data are divided into overlapping 200  $\mu\text{sec}$  segments. Segment S is centered on the pressure fluctuation. The instantaneous value of the pressure during a segment,  $p(t)$ , is compared with the value obtained from the fit for that segment,  $p_f(t)$ ;  $p'(t)$  is given by  $p'(t) = p(t) - p_f(t)$ . The separation between the data shown above,  $\Delta$ , is 200  $\mu\text{sec}$ .  $R(\tau)$  is defined in the text.

Time Lag. The duration of the fluctuation as evidenced in the pressure history is given by  $t_{wp}$ . The simultaneous duration of the fluctuation as evidenced in the interferometer data (F) is given by  $t_{wi}$ . The time lag between the arrival of the contact surface and the appearance of the fluctuation at the optical window in the test section is  $t_D$ . (b) The Inverse of the Time Lag vs Pressure Deviation Strength. The peak value of the pressure in the fluctuation is  $p_B$ . The average value of the pressure immediately before and after the fluctuation is  $p_L$ . The straight line is a least square fit (correlation coefficient = 0.997) to

$w = 1661 Z - 1405$  in which  $w = tD^{-1} \times 10^{-3} \text{ sec}^{-1}$   
and  $Z = p_B/p_L$ . The data in (b) are taken from  
the  $\beta_1$  fluctuation (see text).

Figure 12      Fluctuation Dynamics: Velocity. With the velocity      33  
of the contact surface,  $v_3$  (computed from the  
measured value of  $M_s$ ), and the measured velocity  
of the pressure fluctuation as tracked through two  
consecutive pressure gauge histories,  $v_L$ , then  
 $\Delta v \approx v_3 - v_L$ .

Figure 13      Fluctuation Dynamics: Reynolds Number. (See text.)      34  
The time lag between the appearance of the contact  
surface and the appearance of the large pressure  
fluctuation at the test section's window is  $tD$ .  
The Reynolds number per unit centimeter is computed  
from the measured Mach number  $M_s$  for conditions in  
the driver gas at the contact surface.

Figure 14      Boundary Layer Model:  $\log (1/tD)$  vs  $Re$ . The      38  
Reynolds number is derived from a boundary layer  
model for the contact surface; the quantity  $tD$   
is as defined previously. The dashed lines are  
least squares fits with correlation coefficients  
 $r_{\beta_1} = 0.992$  and  $r_{\beta_2} = 0.998$ . The average slope  
for the two lines is  $m_{Av} = 2.7 \pm 0.7$  where  
 $m = d\{\log (1/tD)\}/d (re)$ .

- Figure 15 Shock Heated Driven Gas Flow Velocity vs. 45  
Driver/Driven Gas Density Ratio. Solid line:  
 $\gamma_1 = 7/5$ ,  $\gamma_4 = 5/3$ . Dashed line:  $\gamma_1 = \gamma_4 = 5/3$ .
- Figure 16 Shock Wave Speed (Arbitrary Units) vs. Driver 47  
Energy Density. (See text for details.)  
o, Menard<sup>3</sup>; o, Gruszczynski and Warren<sup>4</sup>;  
 $\Delta$ , Camm and Rose<sup>4</sup>; x, present measurements.
- Figure 17 Mach Number vs. Initial Driver Tube Pressure. 50  
 $\Delta$ ,  $p_1 = 0.1$  Torr; +,  $p_1 = 0.5$  Torr; o,  $p_1 = 1.0$  Torr;  
o,  $p_1 = 2.0$  Torr; x,  $p_1 = 0.4$  Torr. All data shown  
are for a He/Ar set-up.
- Figure 18 Electrical Conversion Efficiency vs. Initial Driver 51  
Tube Pressure. The data shown in Figure 3 have  
been averaged over  $p_1$ .
- Figure 19 Absorption Coefficient vs. Temperature at a Fixed 62  
Gas Density. (1)  $n = 10^{19} \text{ cm}^{-3}$ ; (2)  $n = 10^{18} \text{ cm}^{-3}$ ;  
(3)  $n = 10^{17} \text{ cm}^{-3}$ ; (4)  $n = 10^{16} \text{ cm}^{-3}$ .
- Figure 20 Absorption Coefficient vs. Temperature at a Fixed 64  
Electron Density. (1)  $n_e = 10^{19} \text{ cm}^{-3}$ ; (2)  $n_e =$   
 $10^{18} \text{ cm}^{-3}$ ; (3)  $n_e = 10^{17} \text{ cm}^{-3}$ ; (4)  $n_e = 10^{16} \text{ cm}^{-3}$ .
- Figure 21 Absorption Coefficient vs. Electron Density at a 65  
Fixed Temperature. (1)  $T = 12,000^\circ\text{K}$ ; (2)  $T = 18,000^\circ\text{K}$ ;  
(3)  $T = 24,000^\circ\text{K}$ .

## I. Introduction

We have been motivated to investigate alternatives to the phenomenological approach to turbulence by the well-known deficiencies in that approach. These deficiencies include: (1) the use of empirical constants not derivable from the fundamental constants of nature; (2) the inability to consistently explain the existence and systematics of large coherent structures in "steady" turbulence; (3) the inadequate characterizations of transport effects observed in reacting transitional flow, especially, flow with exothermic processes; (4) the incomplete statistical description of the randomly fluctuating gasdynamical variables. Generally stated, we have sought to create and understand turbulent environments where phenomena might be observed which would allow us to distinguish and evaluate new approaches to turbulence. In parallel with these efforts, we have sought to extend the new approaches into regimes which are accessible to our measurement capabilities. This report reviews the principal specific results within that general context from our beginning two year studies of turbulence with NASA support.

## II. Reaction Rate Distortion in Turbulent Flow

Consider the irreversible chemical reaction  $A + B \rightarrow P$  in a turbulent gas from a classical point of view. Impact parameters between particles  $\ell$  and  $k$  are  $b_{\ell k}$ , the separation between their centers, and  $\epsilon$ , the angle between their original and final velocities in the center of mass. Each particle has a characteristic mass  $m$  and a characteristic internal energy  $E_\ell$ . Let's assume that: (1) interactions are unimportant; (3) only binary collisions need be considered. Mass and total momentum are to be strictly conserved in all collisions. Energy is also conserved; however, the product  $P$  is produced in an excited state (with excess internal energy  $E_{p*}$ ) from which it very promptly relaxes to its characteristic internal state  $E_p$  through some unspecified noncollisional (radiative) process. We shall apply the approach used by Tsugé<sup>1</sup> to this problem as we look for an explicit influence of turbulence on the apparent reaction rate.

Using the Klimontovich  $N$ -particle distribution function<sup>2</sup> with the six dimensional phase space coordinate  $Z$ ,  $\hat{f}(Z, t) \equiv \sum_{s=1}^N \delta[Z - Z^{(s)}(t)]$ , the Master Boltzmann Equation for  $A$  may be written as:

$$\begin{aligned} \left( \frac{\partial}{\partial t} + \mathbf{v}_A^r \cdot \frac{\partial}{\partial \mathbf{x}^r} \right) \hat{f}_A^0 = \sum_{\ell} \left\{ \left( \hat{f}_A^0 \hat{f}_\ell^0 - \hat{f}_A^0 \hat{f}_\ell^0 \right) |\vec{v}_A - \vec{v}_\ell| b_{A\ell} db_{A\ell} d\epsilon d^3 \hat{v}_\ell \right\} \\ - \int (F) \hat{f}_A^0 \hat{f}_B^0 |\vec{v}_A - \vec{v}_B| b_{AB} db_{AB} d\epsilon d^3 \hat{v}_B \end{aligned} \quad \text{II-(1)}$$

where  $\ell = A, B$ , then  $P$  and the function "F" is the fraction of collisions between A and B which result in formation of P. The equation for B is the same as II-(1) with the B label replacing A:

$$\left(\frac{\partial}{\partial t} + \mathbf{v}_B^r \frac{\partial}{\partial \mathbf{x}^r}\right) \hat{f}_B^{\circ} = \sum_{\ell} \{ (B \rightarrow A \text{ above}) \} - \int (F) \hat{f}_B^{\circ} \hat{f}_A^{\circ} |\vec{v}_B - \vec{v}_A| b_{AB} db_{AB} d\epsilon d^3 \hat{v}_A$$

II-(2)

For the product P:

$$\begin{aligned} \left(\frac{\partial}{\partial t} + \mathbf{v}_P^r \frac{\partial}{\partial \mathbf{x}^r}\right) \hat{f}_P^{\circ} = & \sum \left\{ \left( \hat{f}_P^{\circ} \hat{f}_{\ell}^{\circ} - \hat{f}_P^{\circ} \hat{f}_{\ell}^{\circ} \right) |\vec{v}_P - \vec{v}_{\ell}| b_{P\ell} db_{P\ell} d\epsilon d^3 \hat{v}_{\ell} \right\} \\ & + \int (F) \hat{f}_A^{\circ} \hat{f}_B^{\circ} |\vec{v} - \vec{v}_B| \partial (m_A \vec{v}_A + m_B \vec{v}_B - m_P \vec{v}_P) b_{AB} db_{AB} d\epsilon d^3 \hat{v}_A d^3 \hat{v}_B \end{aligned}$$

II-(3)

Equation II-(1) simply says that the rate of change in the number of molecules in a phase-space volume element  $d^3 x d^3 v_A$  is equal to the sum of the differences of the rate of molecule A into and out of the specified volume element due to collisions between: A and A; A and B; A and P; less the rate resulting from the formation of P. Equation II-(2) has the same meaning for molecule B. Equation II-(3) is different since there are no collisions involving P which can cause the reaction; however, a fraction of the collisions of A and B do produce P. The inclusion of a delta function is to insure that only those collisions which conserve momentum are allowed and to guarantee



that the resulting new P molecules will be in the specified volume element  $d^3x d^3v_P$  around  $\vec{x}$  and  $\vec{v}_P$ .

Following Tsugé, we can define:  $\bar{f} = f$ ;  $\hat{f}_A \hat{f}_B = f_{AB}(Z_A, \hat{Z}_B)$

$$\begin{aligned} \hat{f}_A \hat{f}_A &= \sum_{s=1}^N \delta[Z_A - Z_A^{(s)}(t)] \sum_{s=1}^N \delta[Z_A - Z_A^{(\hat{s})}(t)] = \sum_{s \neq s}^N \delta[Z_A - Z_A^{(s)}(t)] \delta[Z_A - Z_A^{(\hat{s})}(t)] \\ &+ \delta(Z_A - \hat{Z}_A) \sum_{s=1}^N \delta[Z_A - Z_A^{(s)}(t)] = f_{AA}(Z_A, \hat{Z}_A) + \delta(Z_A - \hat{Z}_A) f_A(Z). \end{aligned}$$

Turbulent-like effects are obtained without ad hoc assumptions from situations where, defining  $\psi(Z, \hat{A}) \equiv f^{II}(Z, \hat{Z}) - f(Z)f(\hat{Z})$ , one finds a history with  $\psi(Z, Z) \neq 0$ . The importance of this approach to turbulent flow without reactions has already been discussed.<sup>3</sup>

By taking the averages of equations II-(1), II-(2), and II-(3) and then, in turn, multiplying each equation by a moment function  $\alpha(\vec{v}_\ell) = \alpha_\ell$  and integrating over  $d^3v_\ell$ , we can add the three resulting equations and find (using standard notation):

$$\begin{aligned} \sum_{\ell} \left\{ \frac{\partial}{\partial t} \int \alpha_{\ell} f_{\ell} d^3v_{\ell} + \frac{\partial}{\partial x^r} \int \alpha_{\ell} v_{\ell}^r f_{\ell} d^3v_{\ell} - \int \left( \frac{\partial \alpha_{\ell}}{\partial t} + v_{\ell}^r \frac{\partial \alpha_{\ell}}{\partial x^r} \right) f_{\ell} d^3v_{\ell} \right. \\ = \sum_{k, \ell} \left\{ \frac{1}{2} (\alpha_{\ell} + \alpha_k - \alpha_{\ell} - \alpha_k) [f_{\ell} \hat{f}_k + \psi_{\ell k}(Z_{\ell}, \hat{Z}_k)] d^3v_{\ell} d^3v_k d^3K_{\ell k} \right\} \\ + \int \alpha_P(F) [f_A \hat{f}_B + \psi_{AB}(Z_A, \hat{Z}_B)] \delta(m_A \vec{v}_A + m_B \vec{v}_B - m_P \vec{v}_P) d^3v_A d^3\hat{v}_B d^3v_P d^3K_{AB} \\ - \int (\alpha_A + \alpha_B)(F) [f_A \hat{f}_B + \psi_{AB}(Z_A, \hat{Z}_B)] d^3v_A d^3\hat{v}_B d^3K_{AB} \end{aligned} \quad \text{II-(4)}$$

where  $k$  also stands for  $A$ ,  $B$ , or  $P$ , and  $d^3K_{AB} = |\vec{v}_A - \vec{v}_B| b_{AB} db_{AB} d\epsilon$ .

Now we can define, in the usual manner and again using standard notation, the hydrodynamical quantities of interest:

$$n_\ell = \int f_\ell d^3v_\ell, \quad \rho = \sum_\ell m_\ell n_\ell, \quad \vec{u}_\ell = \frac{1}{n_\ell} \int \vec{v}_\ell f_\ell d^3v_\ell, \quad \vec{u} = \frac{1}{\rho} \sum_\ell n_\ell m_\ell \vec{u}_\ell;$$

$$\vec{\xi}_\ell \equiv \vec{u}_\ell - \vec{u} = \frac{1}{n_\ell} \int (\vec{v}_\ell - \vec{u}) f_\ell d^3v_\ell = \frac{1}{n_\ell} \int \vec{c}_\ell f_\ell d^3v_\ell, \quad \vec{c}_\ell \equiv \vec{v}_\ell - \vec{u};$$

$$n = \sum_\ell n_\ell, \quad E = (\sum_\ell n_\ell E_\ell)/n, \quad 3KT/2 = (\sum_\ell m_\ell \int c_\ell^2 f_\ell d^3v_\ell)/2n;$$

$$P_{ij}^\ell \equiv m_\ell \int c_\ell^i c_\ell^j f_\ell d^3v_\ell, \quad P_{ij} = \sum_\ell P_{ij}^\ell; \text{ and } q_i = \sum_\ell \int c_\ell^i \left( \frac{m_\ell c_\ell^2}{2} + E_\ell \right) f_\ell d^3v_\ell.$$

When  $\alpha_\ell = m_\ell$  and  $\alpha_\ell^i = m_\ell v_\ell^i$  Equation II-(4) becomes, using the definitions above:

$$\frac{\partial \rho}{\partial t} + \frac{\partial}{\partial x^r} (\rho u^r) = 0 \quad \text{and} \quad \frac{\partial (\rho u^i)}{\partial t} + \frac{\partial}{\partial x^r} [P_{ir} + \rho u^i u^r] = 0$$

respectively since mass and momentum are strictly conserved.

Thus, these conservation equations are unchanged from their usual appearance even for inelastic collisions. When

$\alpha_\ell = \frac{1}{2} m_\ell v_\ell^2 + E_\ell$ , the summation term on the right hand side of equation (4) is zero due to strict conservation of energy in the elastic collisions. The remaining terms on the right hand side are:

$$\begin{aligned}
& \int \left[ \frac{(m_A \vec{v}_A + m_B \vec{v}_B)^2}{2m_P} + E_P \right] (F) [f_A \hat{f}_B + \psi_{AB}(z_A, \hat{z}_B)] d^3 \vec{v}_A d^3 \hat{\vec{v}}_B d^3 K_{AB} \\
& - \int \left( \frac{m_A v_A^2 + m_B \hat{v}_B^2}{2} + E_A + E_B \right) (F) [f_A \hat{f}_B + \psi_{AB}(z_A, \hat{z}_B)] d^3 \vec{v}_A d^3 \hat{\vec{v}}_B d^3 K_{AB} \\
& = \int [E_P - E_A - E_B - \frac{1}{2} \mu \mathbf{V}^2] (F) [f_A \hat{f}_B + \psi_{AB}(z_A, \hat{z}_B)] d^3 \vec{v}_A d^3 \hat{\vec{v}}_B d^3 K_{AB}
\end{aligned}$$

where  $\mu = m_A m_B / (m_A + m_B)$  and  $\mathbf{V} = |\vec{v}_A - \vec{v}_B|$ . Evaluating the left hand side of the equation (4), we achieve

$$\begin{aligned}
& \frac{\partial}{\partial t} \left[ \frac{3}{2} nkT + \frac{1}{2} \rho u^2 + nE \right] + \frac{\partial}{\partial x^r} \left[ \frac{1}{2} \rho u^2 u^r + \frac{3}{2} nkT u^r + P_{ir} u^i + q_r + nE u^r \right] \\
& = \int [E_P - E_A - E_B - \frac{1}{2} \mu \mathbf{V}^2] (F) [f_A \hat{f}_B + \psi_{AB}(z_A, \hat{z}_B)] d^3 \vec{v}_A d^3 \hat{\vec{v}}_B d^3 K_{AB} \quad \text{II-(5)}
\end{aligned}$$

Of course, the reaction is prohibited when  $E_P - E_A - E_B > \frac{1}{2} \mu \mathbf{V}^2$ . If  $E_P > E_A + E_B$  but  $E_P - E_A - E_B < \frac{1}{2} \mu \mathbf{V}^2$ , then part of  $\frac{1}{2} \mu \mathbf{V}^2$  is used to increase the internal energy of the system and the remainder is released in the form of heat. If  $E_P < E_A + E_B$ , then heat is produced in the amount  $(E_A + E_B + \frac{1}{2} \mu \mathbf{V}^2 - E_P)$  with each reaction. Equation II-(5) is consistent with these expectations since the energy dependence is contained in "F".

Our new result is contained in the term with a contribution from  $\psi_{AB}(z_A, \hat{z}_B)$ . Equation II-(5) asserts that, when the reaction is allowed ( $F \neq 0$ ), it can be affected by turbulence in a direct manner which is distinguishable from that arising from ordinary turbulent diffusion. A new apparent reaction rate fraction,  $F_{App}$ , can be defined:

$$F_{\text{App}} \equiv \frac{(F) [f_A \hat{f}_B + \psi_{AB}(Z_A, \hat{Z}_B)]}{f_A \hat{f}_B}, \text{ and } \frac{F_{\text{App}} - F}{F} = \frac{\psi_{AB}(Z_A, \hat{Z}_B)}{f_A \hat{f}_B}$$

Thus, there is an explicit influence of turbulence on the rate of production of P; the reaction is distorted in all cases where the condition  $(\psi_{AB}/f_A \hat{f}_B \ll 1)$  is violated.

### III. Turbulent Bursts in a Shock Tube

Turbulent discontinuities in shock tubes are usually thought to be boundary layer-like insofar as transition to turbulence is concerned.<sup>4</sup> However, theoretical treatments which rely on the techniques from linear stability formulations have seemed to be inadequate for the analysis of instabilities in contact surfaces<sup>5</sup> and detonation fronts.<sup>6</sup> Tsugé's treatment,<sup>7</sup> by contrast, is not restricted to the small perturbation regime; macroscopic turbulent effects are shown to evolve from a kinetic theory with reduced microscopic (molecular) chaos. Furthermore, transition related turbulent bursts in a Blasius boundary layer experiment are successfully interpreted.<sup>7</sup> Here in this paper, we suggest an extension of Tsugé's approach to a wider class of unstable boundary layers, viz., to analogous unstable gasdynamic discontinuities in shock tubes.

When one focuses on those fluctuations which experience maximum amplification and identifies these fluctuations as the experimentally observed fluctuations, the theoretical solutions dictate the familiar form

$$I = \exp[\phi(\text{Re}, \lambda)]. \quad \text{III-(1)}$$

Solutions of equation III-(2) are well known.<sup>7,8,9</sup> The Reynolds number has its usual meaning. The expansion parameter  $\lambda$  has the units of frequency. The quantity  $I$  is an explicit function of turbulent intensity,  $I \equiv Q/Q_0$ , where  $Q$  is the observed turbulent

intensity and  $Q_0$  is a minimum intensity level which must be exceeded in order for fluctuations to grow. The function  $\phi$  has no empirical constants; all constants are derivable from boundary conditions. Therefore, this formulation is non-phenomenological and has unique physical consequences. <sup>10,11</sup>

If one considers the solutions of equation II-(1) in the form of a family of curves of  $I'$  vs  $Re$  (where  $I' = \log I$ ) at selected values of the nondimensional ratio  $\lambda v/u_d^2$  ( $v$  is the kinematic viscosity and  $u_d$  is a characteristic free stream boundary layer velocity), systematic behaviors emerge. The curves show: a first regime with  $(dI'/dRe) > 0$ ,  $(d^2I'/dRe^2) > 0$ ; a middle regime which is essentially linear, with  $(dI'/dRe) > 0$ ,  $(d^2I'/dRe^2) = 0$ ; and a third regime with  $(dI'/dRe) > 0$  initially and  $(d^2I'/dRe^2) < 0$ . The linear middle regime has a slope which we shall name  $m$  and an intercept on the  $Re$  axis which we name  $Re_n$ . Extrapolated to  $I' = 0$ , the middle regime gives, at  $Re = Re_n$ ,  $Q = Q_0$ . The third regime has a maximum in  $I'$  of value  $I'_{mx}$  at a Reynolds number which we now name  $Re_p$ .

The extension of this kinetic theory of turbulence to any given set of experimental data on unstable boundary layer flow with turbulent bursts is therefore straightforward. If there is a linear regime in a plot of  $\log Q_{(exp)}$  vs  $Re$ , then the slope of the line should be well estimated by a  $m$  appropriate for the Reynolds number range being treated. If there is a maximum in the  $Q'_{(exp)}$  ( $= \log Q_{(exp)}$  vs  $Re$  trajectory), then the value of  $Re$  at  $Q'_{(exp),mx}$  is a measure of  $Re_p$ . One obtains from the measure of  $Re_p$  an estimate of  $\lambda$  (from  $\lambda v/u_d^2$ ), which

can be called the characteristic frequency of the instability, and in turn an estimate of  $Re_n$ . Since in the linear regime the experimental data will fit  $\log Q = b + (m) (Re)$ , the estimate of  $Re_n$  gives an estimate of  $Q_0$  by

$$\log Q \Big|_{Re=Re_n} = \log Q_0 = b + m \cdot Re_n \quad \text{III-(2)}$$

For example, for Shubauer's experiment (as reported in reference 1) the solutions to equation III-(1) in the appropriate Reynolds number range show: a slope  $m$  in the second regime independent of  $\lambda$ , i.e.,  $m \neq m(\lambda)$  and  $m \approx (dI'/dRe) = (3.3 \pm 0.2) \times 10^{-3}$ ; a systematic dependence of the characteristic wavelength on  $Re_p$  from the third regime which is given by  $(\lambda v/u_d^2) = (4.6 \pm 0.3) \times 10^{-5} \times \exp[-(0.34 \pm 0.02) \times 10^{-3} Re_p]$ ; a correlation between  $Re_n$  and  $Re_p$  which is found to be  $Re_n = (0.29 \pm 0.06) + (0.44 \pm 0.02) Re_p$ . In the data with turbulent bursts, a linear regime is found with slope  $m_{(exp)} = dQ'/dRe = 3.5 \times 10^{-3}$  and a  $Q'$ -axis intercept  $b_{(exp)} = -11.45$ . A maximum in the  $Q'$  vs  $Re$  plane occurs at  $Re_p = 3.19 \times 10^3$ ; this gives  $(\lambda v/u_d^2) = 1.55 \times 10^{-5}$  from the expression above in agreement with the results in reference 1. In addition, using the  $Q'$  axis intercept and the relationship between  $Re_n$  and  $Re_p$  (which provides  $Re_n = 1.4 \times 10^3$ ) given above, our estimate of  $Q_0$  from equation III-(2) is  $Q_0 = 1.5 \times 10^{-3}$ . This corresponds to  $Q_{mx}/Q_0 = 120$ , i.e., a required minimum turbulent intensity level which is 120 times smaller than the observed maximum intensity in the turbulent bursts.

Consider next a curved unstable detonation wave moving in a shock tube with constant velocity  $u_0$ . The non-one dimensional nature of this discontinuity is assumed (as is now conventional) to have resulted from the shear induced by the curvature related dynamics. Let's model the turbulent front by an apparent boundary layer which is transverse to and symmetric about the axis of propagation. That is, its smallest dimension is at the center of the tube; its largest dimensions (small with respect to the radius of curvature of the front) are at the shock tube's walls. This apparent boundary layer is perpendicular to the "normal" boundary layer at the shock tube's walls. The local Reynolds number in it can be defined using a measured local characteristic length, an overall characteristic kinematic viscosity, and an overall apparent characteristic "free stream" transverse boundary layer velocity  $u_d \approx u_0 (\alpha^2/8)$  arising from the curvature where  $\alpha$  is the total angle subtended by the curved front.

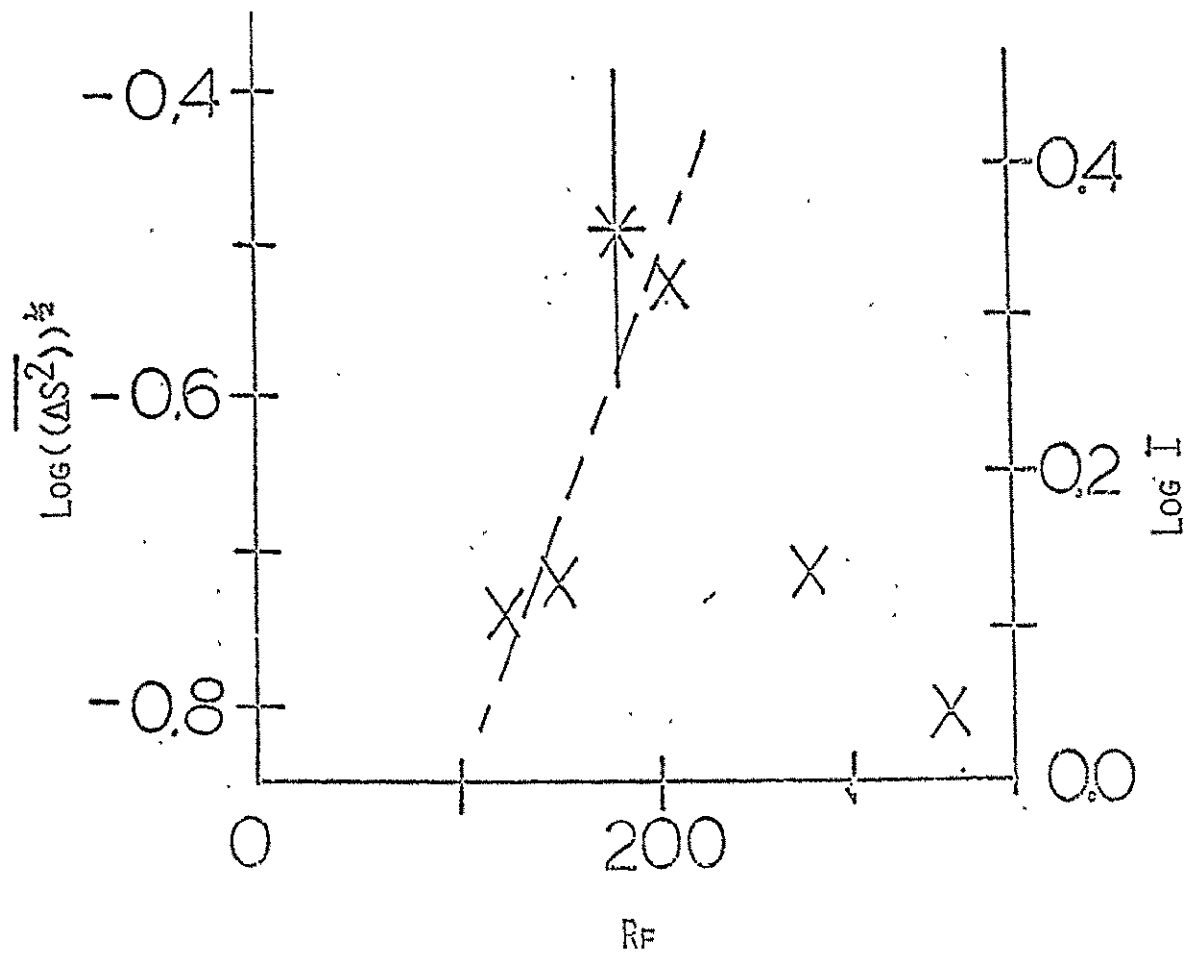
12

White's turbulent detonation wave experiments are amenable to this extension. Measurements of turbulent fluctuation levels and local characteristic lengths are obtained from fringe shift fluctuations in his interferograms using well-known procedures. 13

Specifically, for a self-sustaining detonation into  $2H_2 + O_2 + 2CO$  with  $u_0 = 2.19$  km/s and  $\alpha = 0.047$  rad, turbulent bursts are observed for which  $m_{(exp)} = 3.2 \times 10^{-3}$  and  $Re_p = 208$ . This provides  $(\lambda v/u_d^2) = 4.3 \times 10^{-5}$ . In addition, the fit to the linear regime and the calculated  $re_n (= 92)$  give a ratio of maximum observed intensity to minimum required intensity  $Q_{mx}/Q_0 = 2$ . Figure 1 shows these results.



Thus might a wide variety of discontinuities with similar nonlinear instabilities be treated. We notice that, in the two instances above, the values of  $Q_{mx}/Q_0$  are quite different. This implies radically different turbulence producing mechanisms, an implication which is qualitatively consistent with our intuition. However, it remains to explore similarly obtained values of  $Q_{mx}/Q_0$  and  $(\lambda v/u_d^2)$  for other unstable systems before new quantitative insight can be derived.



1.

#### IV. Driver Gas Flow with Fluctuations

##### A. Introduction

The conventional Navier Stokes equations do not adequately describe turbulent flow. None of the phenomenological approaches which have successfully characterized some turbulent systems seems derivable from a molecular view of matter. On the other hand, a recent series of papers<sup>14,15,16,17</sup> suggests an alternative non-empirical view of turbulence which is based on a modification of the usual view of molecular chaos. A set of modified Navier Stokes equations is derived as well as a variety of unique physical consequences.

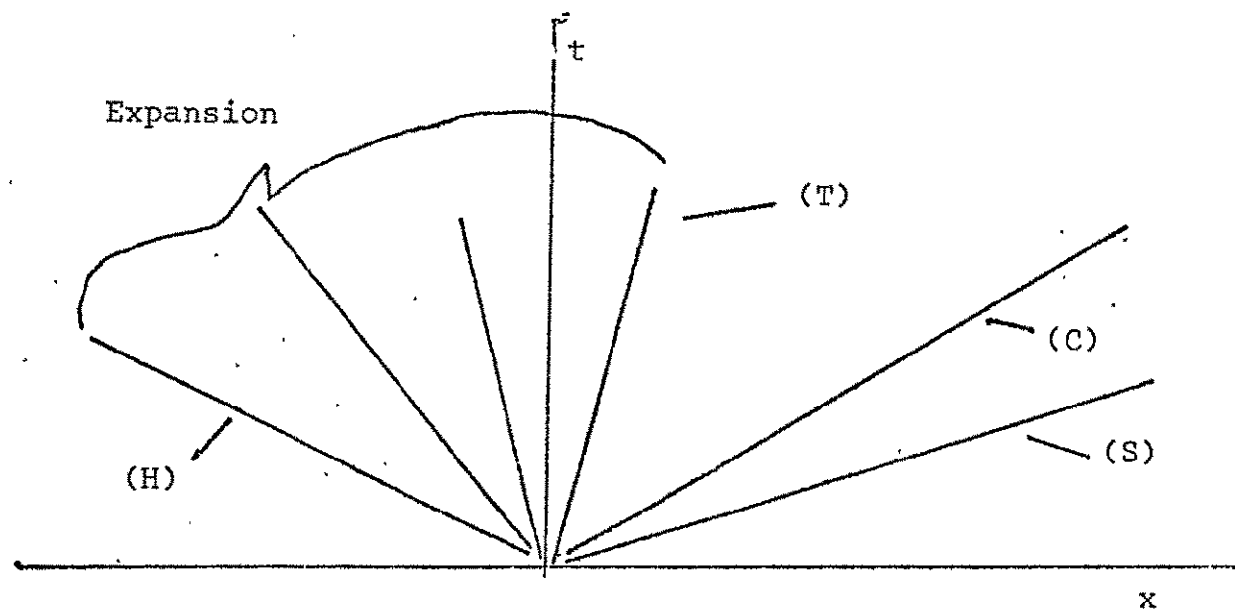
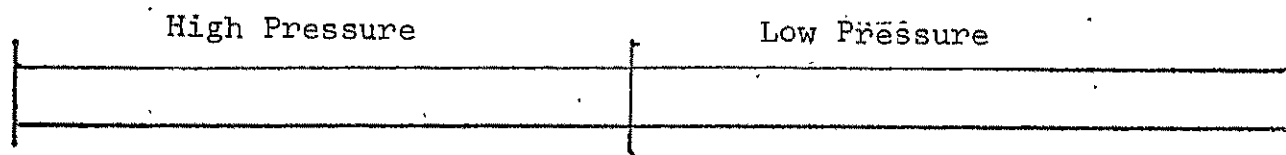
Among these is a characterization of transition to turbulence in boundary layer flow without the usual restriction to linear instabilities. Contact surfaces are ordinarily thought to be boundary-layer like insofar as transition to turbulence is concerned.<sup>18</sup> Linear approaches seem to have failed in many important cases.<sup>19</sup> Therefore, we have explored the potential usefulness of contact surface instabilities in driver gas flow in a shock tube for new insight on turbulence, paying special attention to the possible applicability of the new approach from kinetic theory to our observations.

##### B. Background: Shock Tube Flow

For idealized shock tube calculations, infinitely fast rupture for the diaphragm material separating the high pressure and low pressure sections is usually assumed. (See, for example, Thompson<sup>20</sup> on one dimensional unsteady flow.) This provides the

well-known flow regions indicated in the  $(x,t)$  diagram in Figure 2: a region (1) of un-shocked, driven gas at the original driven gas conditions  $(p_1, T_1, \rho_1)$ ; a region (2) of shock heated driven gas, bounded by the primary shock wave (S), moving at velocity  $w_s$ , on the "downstream" or positive  $x$  side and the contact surface (c) (separating the driven gas from the driver gas), moving at velocity  $v_2$ , on the "upstream" or negative  $x$  side; a region (3) of expansion cooled driver gas; and a region (4) of uncooled stationary driver gas at the original gas conditions  $(p_4, T_4, \rho_4)$ . Between regions (3) and (4), an adiabatic expansion is bounded on the upstream side by the head of the expansion fan moving upstream (i.e., toward negative  $x$ ) at the local speed of sound  $(a_4)$  and, on the downstream side, by the tail of the expansion fan moving at speed  $(v_3 - a_3)$  where  $v_3$  is the local gas velocity  $(= v_2)$ . When  $(v_3 - a_3)$  is positive, the motion of the tail is downstream (i.e., toward positive  $x$ ); cooling of the driver gas persists into the shock tube region downstream of the plane of diaphragm rupture. In the above, the symbols  $p$ ,  $T$ , and  $\rho$  are, as usual, pressure, temperature, and density; the subscripts denote the region. Velocities cited are taken from a laboratory fixed frame of reference.

| The contact surface (C in Figure 2, ideally plane and stable) is inherently unstable<sup>18</sup> against small transverse perturbations. The deviations from one-dimensionality which turbulence implies in turbulent detonation waves are usually thought to be a result from the shear induced by the curvature<sup>21</sup> of the discontinuity. Turbulent contact surfaces also show<sup>20</sup> curvature. In addition, nonuniformities associated with the



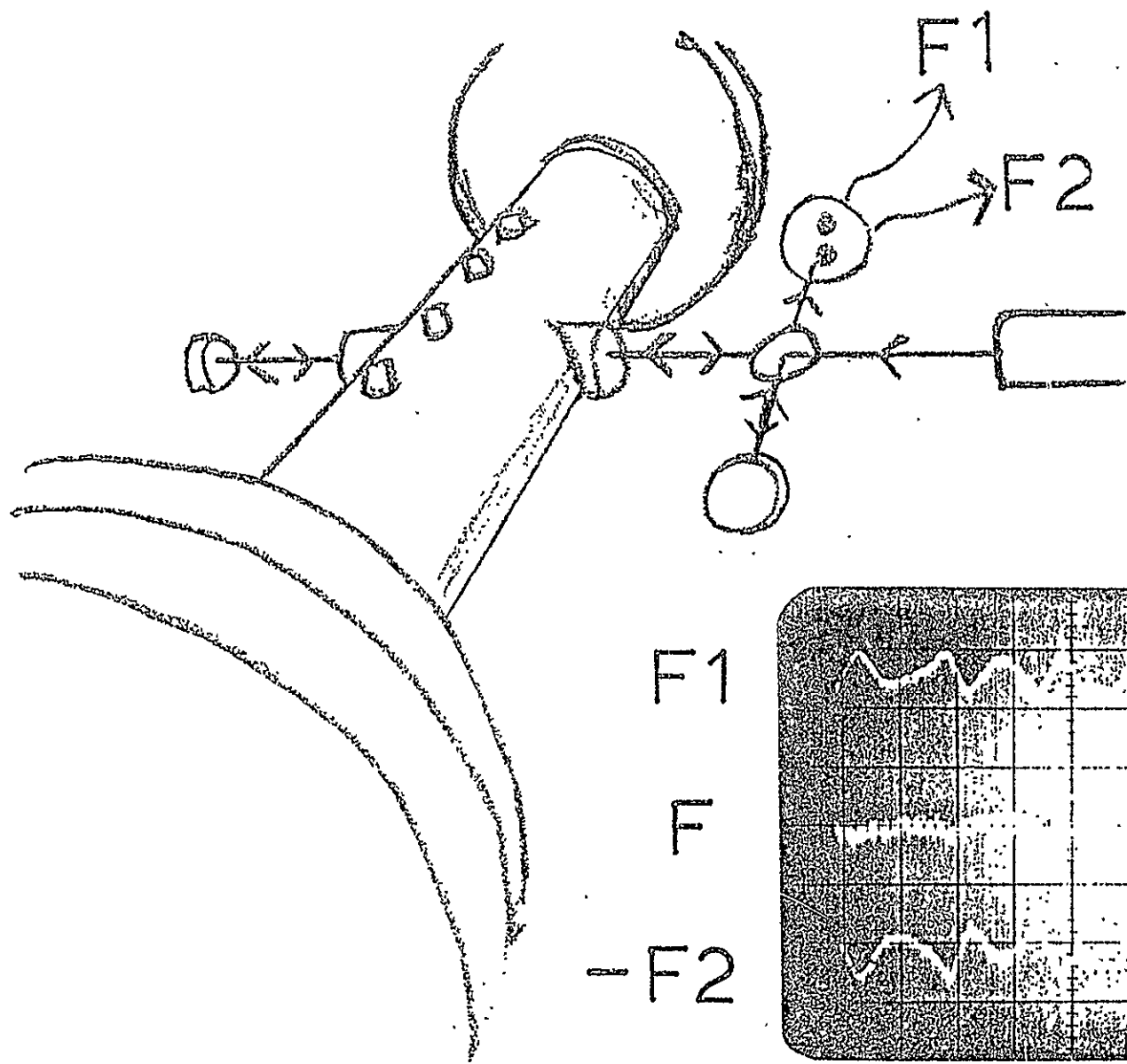
2.

rupture of a diaphragm produce perturbations in the contact surface. Depending on the initial driver gas pressure,  $p_4$ , the local Reynolds number at the contact surface can be made high enough so as to be consistent with the possibility of eventual turbulent flow. Gas particles are accelerated from rest and acquire finally a constant downstream velocity  $v_3$  at the completion of the adiabatic expansion. Furthermore, in the contact surface and wherever else the appropriate conditions exist transition to turbulence can take place.

### C. Apparatus

Our 12.7 cm diameter shock tube's test section has been placed immediately downstream of the diaphragm. High purity  $N_2$  gas (or  $N_2$  with various low concentration  $N_2O_4 \rightleftharpoons 2NO_2$  admixtures) expands adiabatically in the 153 cm long driver tube, after the rupture of a mylar partition, evolving into a low pressure region, the 336 cm long driven tube, also containing  $N_2$  gas. The test section is 153 cm long. Pressure histories are recorded with wall mounted Kistler 606A gauges at the driver section's end plate and at five positions in the test section, including one positioned at its center.

In addition, two 2.5 cm windows at the center of the test section 76.2 cm (downstream) from the diaphragm allow an optical path through the shock tube. In some shock tube firings, this path has allowed us to use blue light absorption ( $0.435 \mu m$ ) from a 200 Watt mercury arc lamp as a diagnostic for  $NO_2$  density. In other firings, the optical path has been used as one arm of a Michelson-Morley interferometer. In both cases, the basic set-up is conventional (see, for example, Bradley<sup>22</sup> for a discussion of these techniques). However, in the latter instance, simultaneous gas density measurements are made possible along two lines equidistant from the diaphragm and a distance one cm apart transverse to the flow of gas in the shock tube. The amplifications and the d-c supply voltages for the two phototubes which are used as fringe shift sensors are adjusted so that, for laminar unsteady low velocity flow, their signals are correlated and cancel when combined. Figure 3 shows a





sketch of the test section and a sample of the interferometer set-up data where ordinary room air flow (resulting from the air-conditioning in our laboratory) has been used.

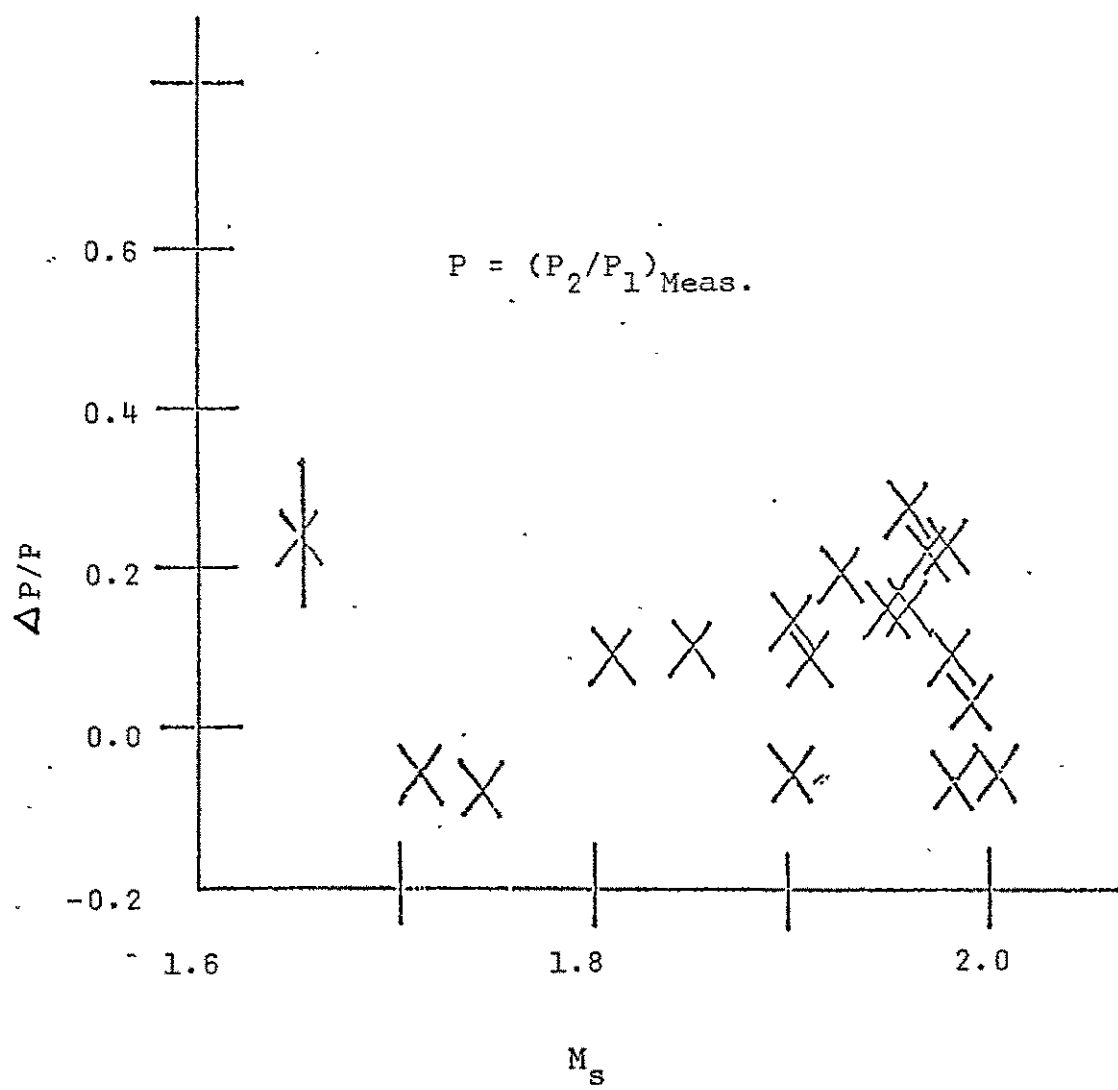
The pressure gauges provide start and stop signals for three time interval counters. Pressure histories,  $\text{NO}_2$  absorption histories and the output from the interferometer (signals  $F_1$ ,  $F_2$  and  $F = F_1 - F_2$ ) are recorded on oscilloscopes with bandwidth  $> 30$  MHz. A Biomation 8100 A to D converter is used in selected instances so that some of our data can be subjected to computer analyses; either the pressure history at the test section window is digitized along with the simultaneous optical data or pressure histories at two different locations are digitized.

## D. Results

### (i) Calibration

We have tested the use of the equations of one-dimensional gasdynamics in our experiments by comparing the measured values of the shock strength ( $p_2/p_1$ ) with the values of  $p_2/p_1$  calculated using the 1-D equations and the measured primary shock wave's Mach number,  $M_s (= w_s/a_1)$ . The range  $1.6 < M_s < 2.1$  is chosen; for a  $N_2/N_2$  system ( $N_2$  as the driver and driven gas) in our shock tube, this range has given us the opportunity of varying the Reynolds numbers in the driver gas at fixed  $M_s$  since  $p_4$  can be varied independently of  $p_4/p_1$  (which determines  $M_s$ ). Figure 4 shows the results from these comparisons. On the average, the measured values of  $p_2/p_1$  are higher than calculated by an amount  $10 \pm 11\%$ ; this effect gives an indication of the limit to which we might reasonably employ the 1-D equations in order to predict flow conditions in the shock wave processed driven gas.

The usefulness of the interferometer data as an indicator of contact surface arrival has also been tested. We monitor the output of one of the two phototubes on which a single fringe has been placed. We observe the sudden change in the fringe shifts to a condition of large (and apparently highly erratic) variations. We define this event as the arrival of the contact surface and measure the time interval which has passed since the arrival of the shock wave at the same point; this time interval is labeled  $T_{c,m}$ . For the same shock tube firing, we use the measured Mach number  $M_s$  to calculate the time interval which would be expected according to the equations of one-dimensional

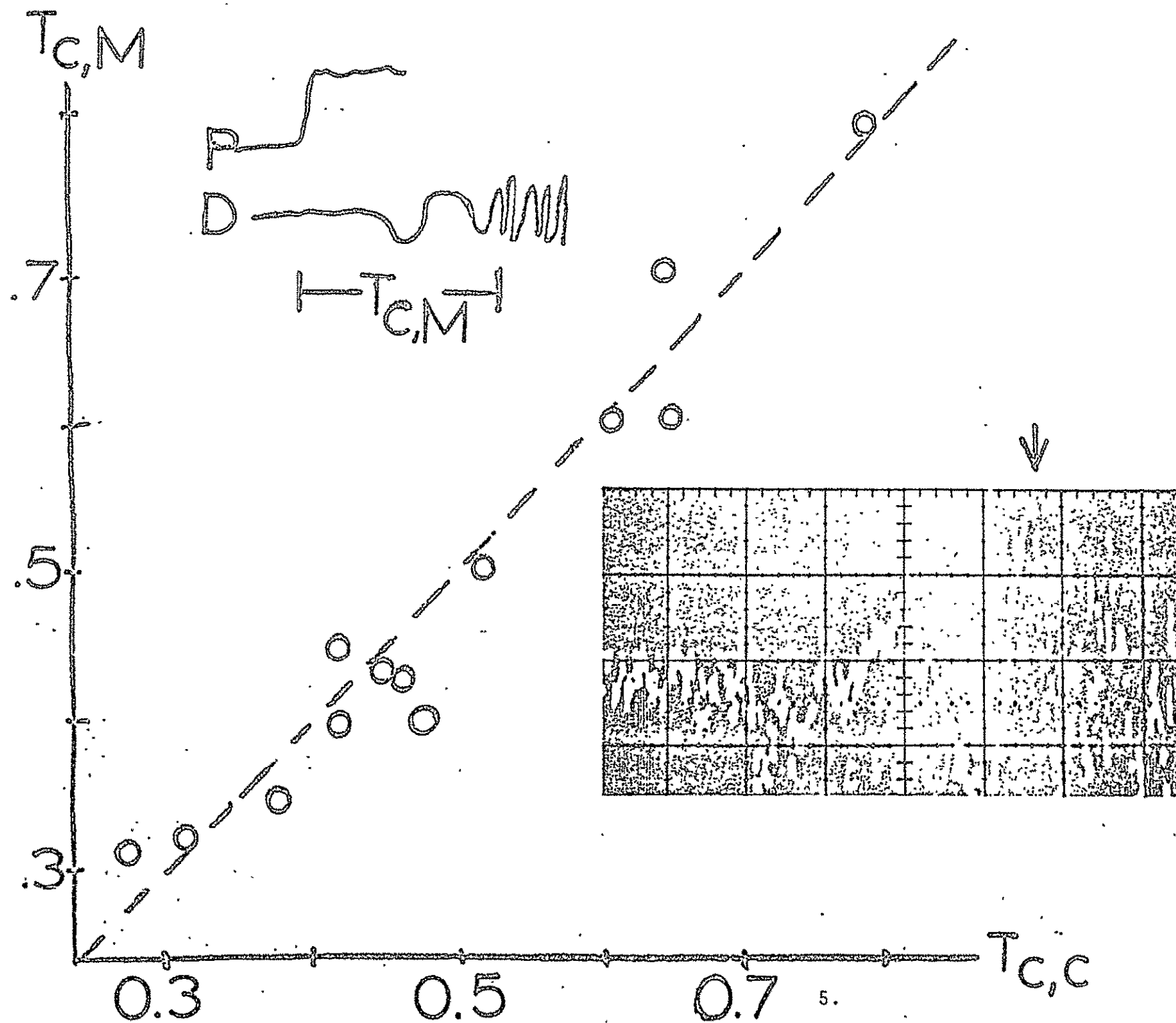


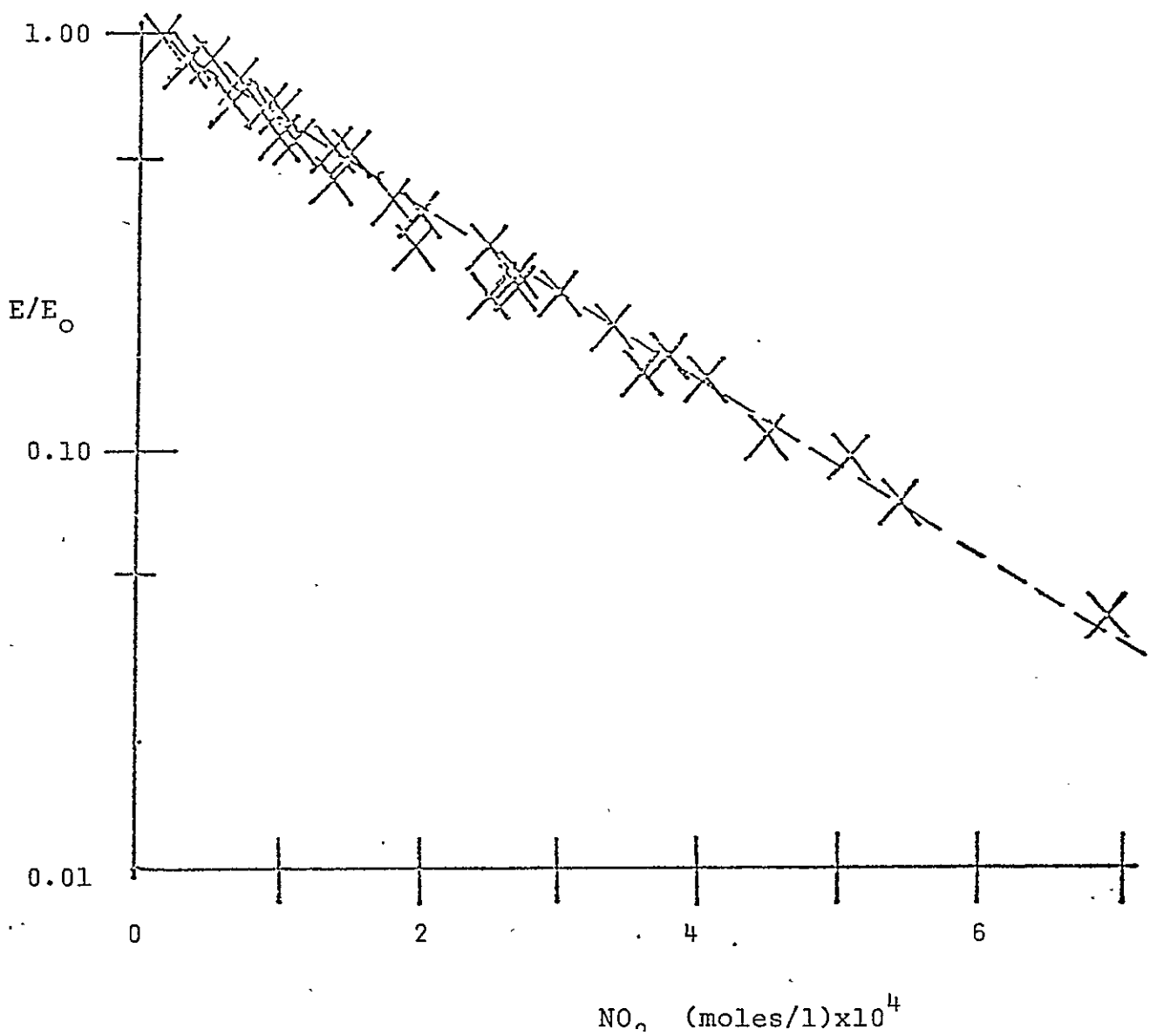
gasdynamics; this time interval is labeled  $T_{c,c}$ . Figure 5 shows comparisons of  $T_{c,c}$  and  $T_{c,m}$ . These data fit a straight line through the origin ( $-1 \pm 42 \mu\text{sec}$ ) with a slope of one ( $0.99 \pm .08$ ) and a correlation coefficient ( $r = 0.97$ ) which is very close to one. Thus, the measured Mach number seems to be an even better predictor of the velocity of the contact surface than it is of the pressure ratio across the shock front.

In addition, we have tested the accuracy of blue light absorption as a diagnostic for  $\text{NO}_2$  density in our set-up. For these calibrations, absorption was measured with a static fill; there was no diaphragm between the driver and driven sections of the shock tube. Lambert-Beer's Law was verified in the form:

$$\log (I/I_0) = a + b [\text{NO}_2]$$

where  $b = \epsilon d$ ,  $\epsilon$  is the extinction coefficient,  $d$  is the path length ( $= 13.97 \text{ cm}$ ) and  $[\text{NO}_2]$  is the  $\text{NO}_2$  density in mole/liter. We found  $a = -(2.9 \pm 11) \times 10^{-3}$  and  $\epsilon = 149. \pm 8 \text{ l/mole-cm}$ . (See Figure 6.) This value of  $\epsilon$  is consistent with previous measurements as reviewed by Zimet.





## (ii) Fluctuations

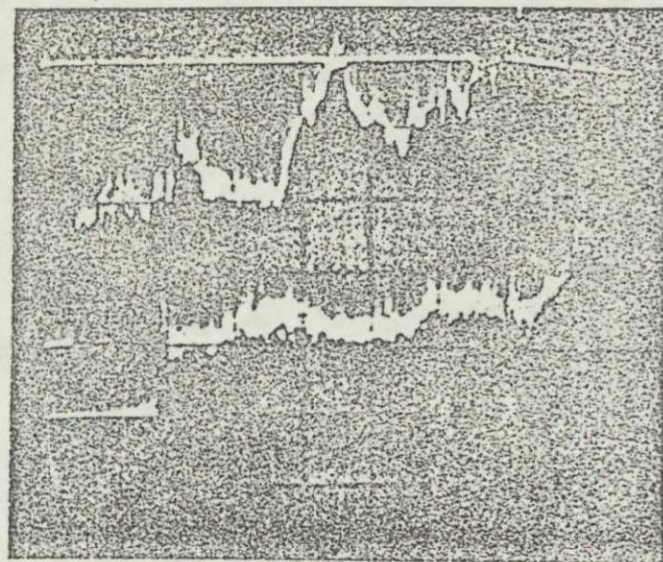
Significant localized deviations from the mean behavior are found in data from the pressure measurements, the interferometer and the blue light absorption. These deviations are found in the driver gas, upstream from the contact surface. The pressure data show large localized variations from the average local pressure. These are associated with a simultaneous change in the behavior of the interferometer output (F) from random variations to a behavior which shows that the density changes sensed by F1 and F2 are strongly correlated. When a low NO<sub>2</sub> concentration mixture is used ( $N_2 + N_2O_4 \rightleftharpoons N_2 + 2NO_2$ ) as the driver gas, the pressure deviations are also associated with simultaneous large decreases in the blue light absorption corresponding to decreases in the NO<sub>2</sub> density. Examples of each of these are shown in Figures 7, 8 and 9.

The statistical behavior of the pressure history has been studied. We use the correlation function  $R(\tau)$ :

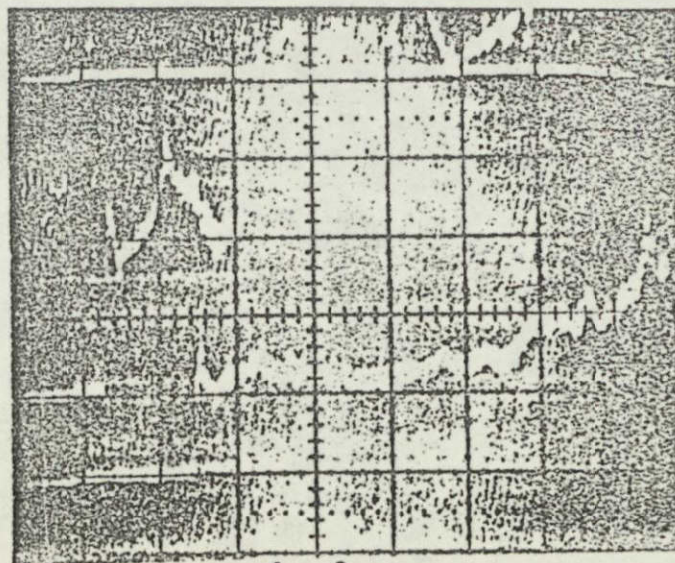
$$R(\tau) = \overline{p'(t)p'(t+\tau)} / \overline{p'(t)^2} ,$$

where  $p'(t)$  is the difference between the instantaneous pressure and the average pressure at time  $t$ . When we compare pre- and post-fluctuation pressure data with data obtained during the fluctuation, the correlation function appears to be structured for data in the fluctuation and unstructured for data before and after the fluctuation. A sample of this is shown in Figure 10. The behavior of  $R(\tau)$  during the fluctuation is consistent with the behavior expected in turbulent flow.

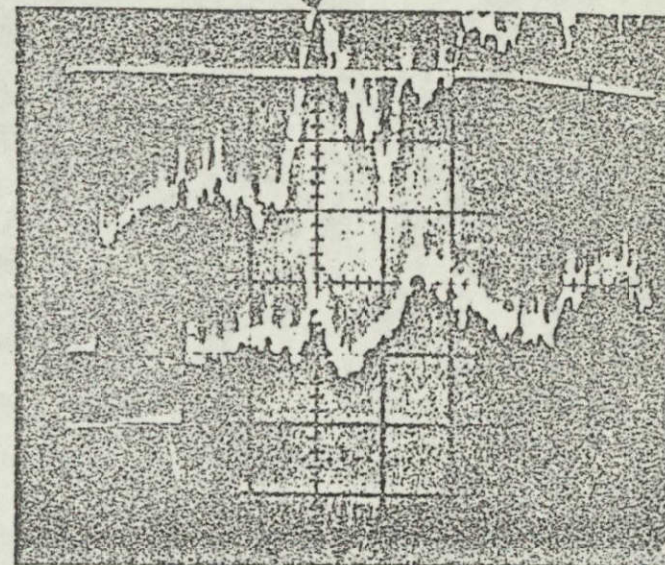




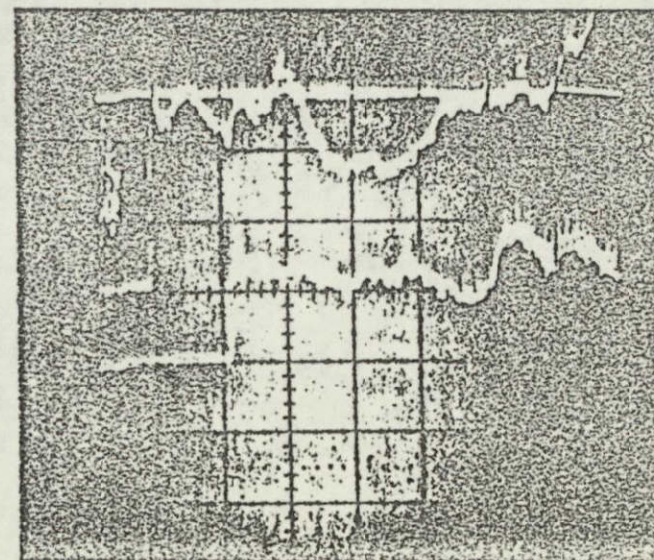
(a)



(b)

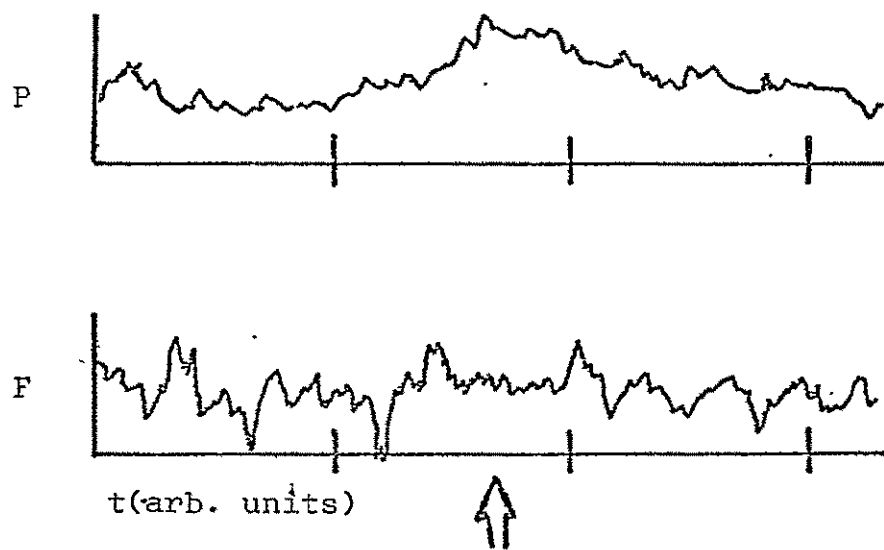


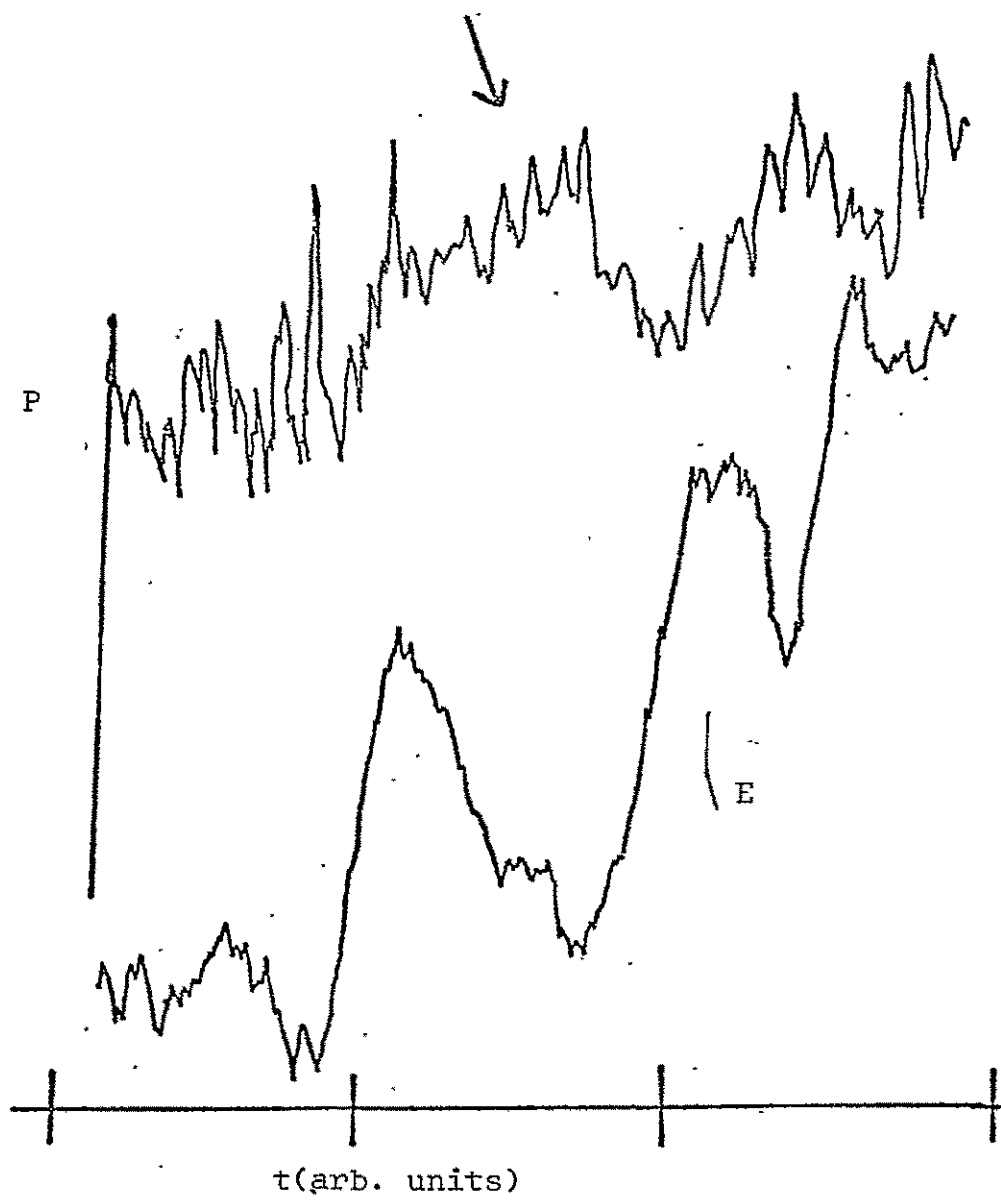
(c)

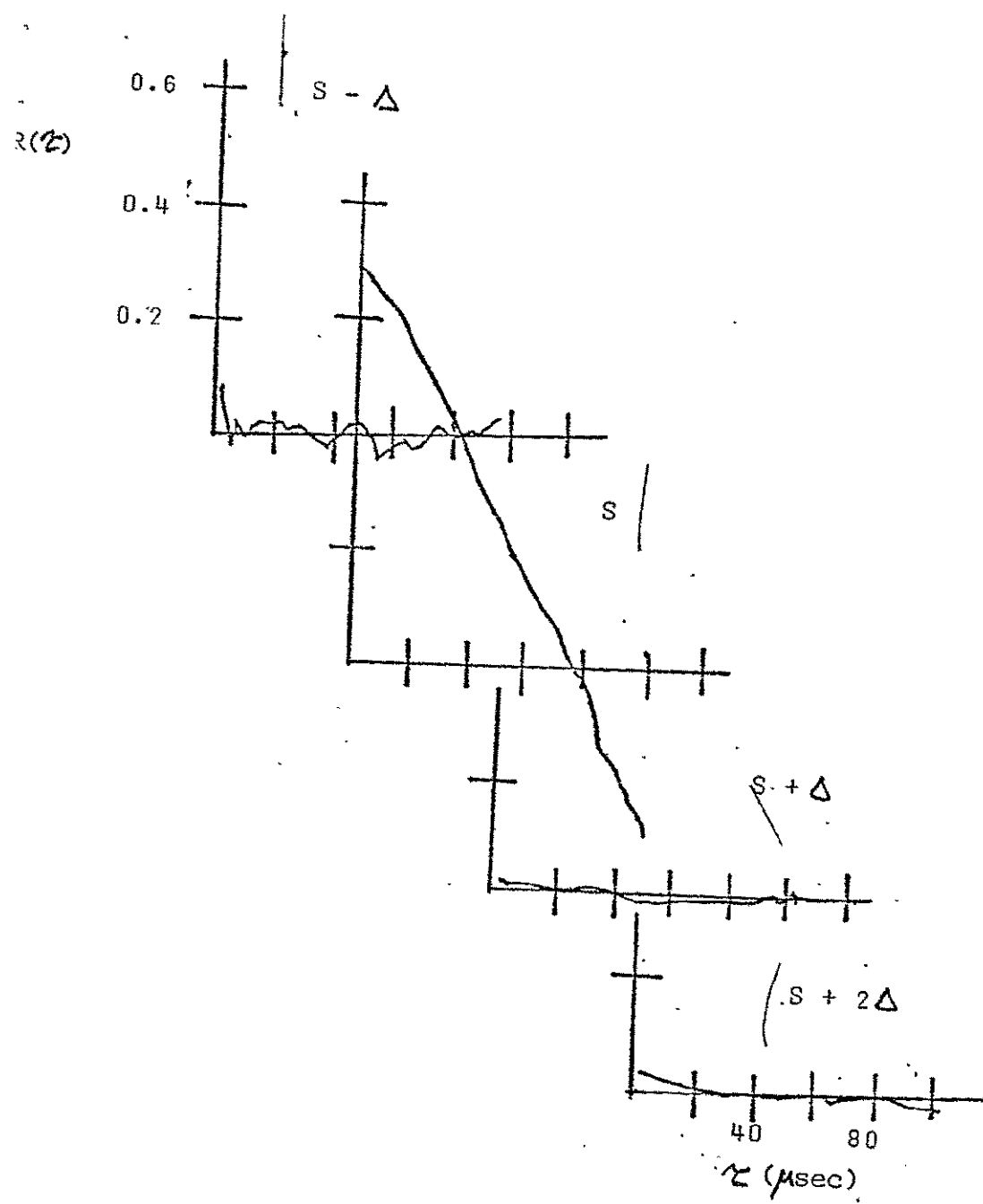


(d)

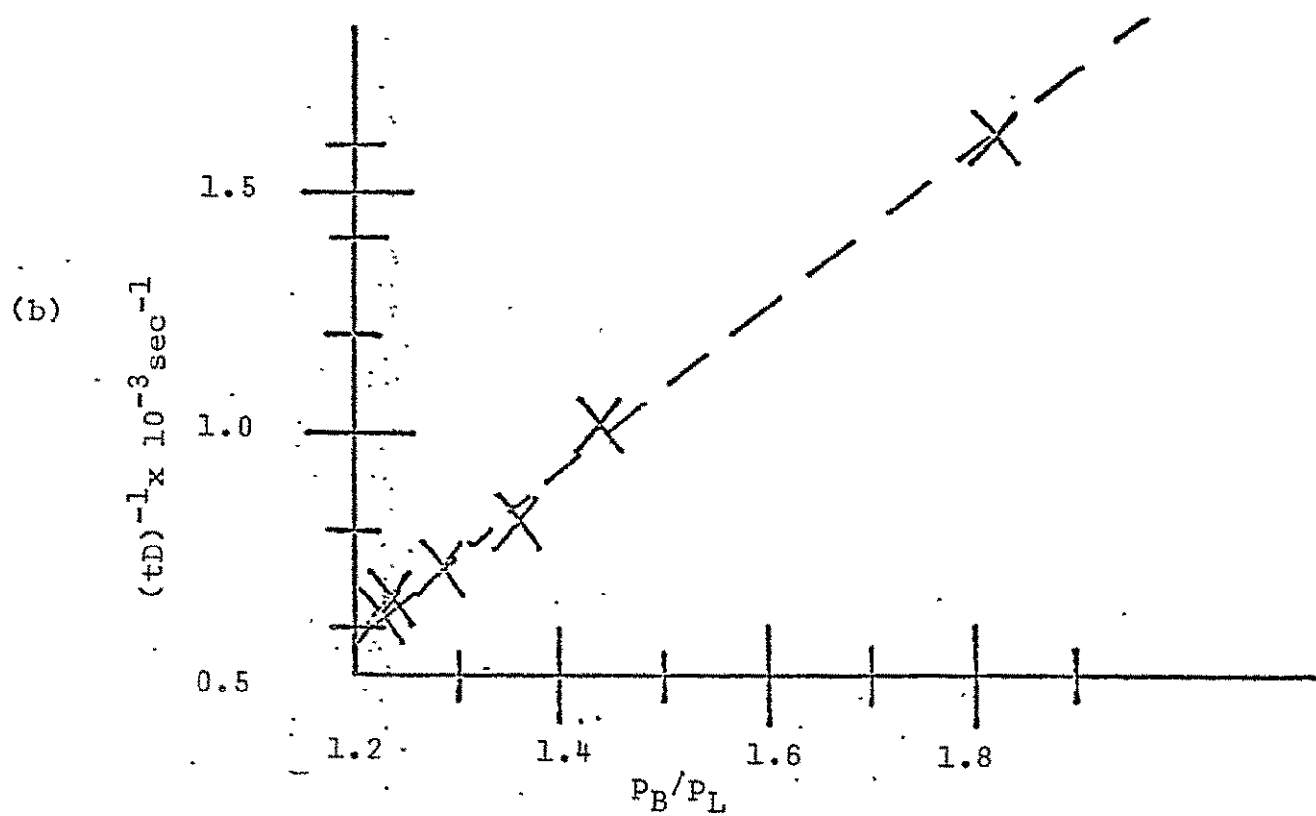
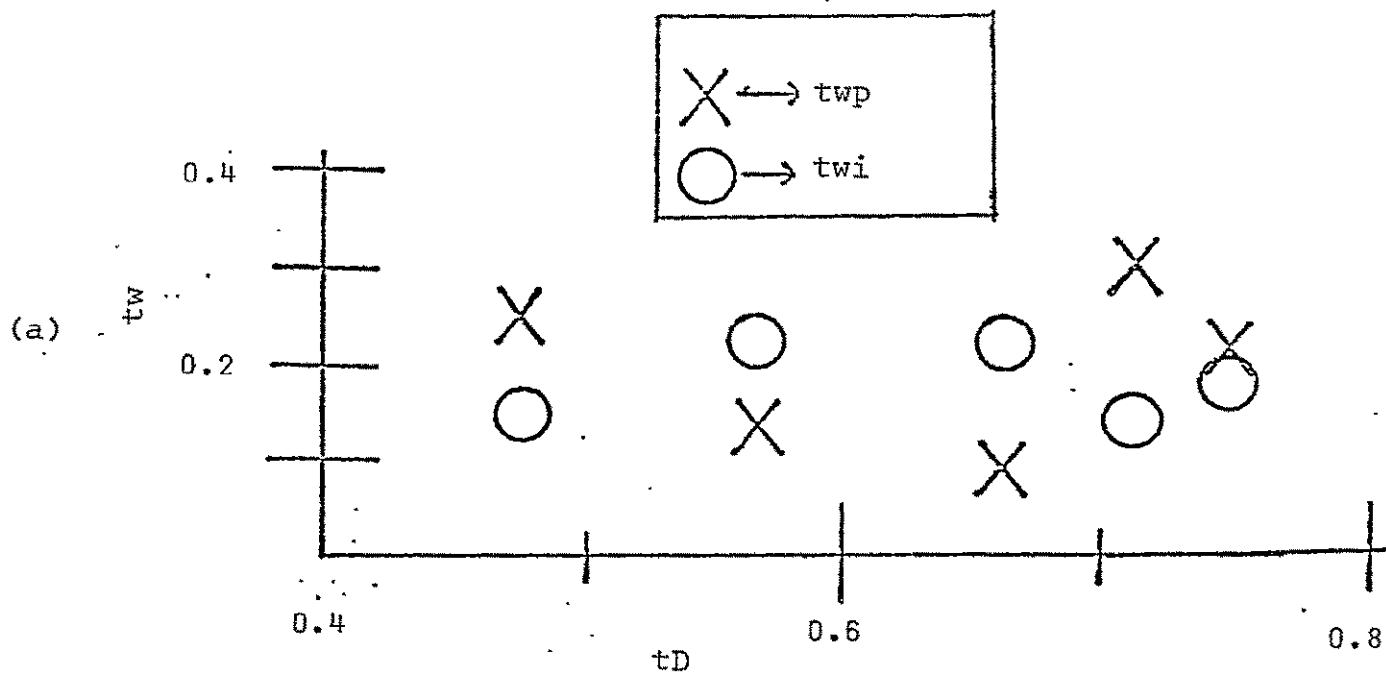


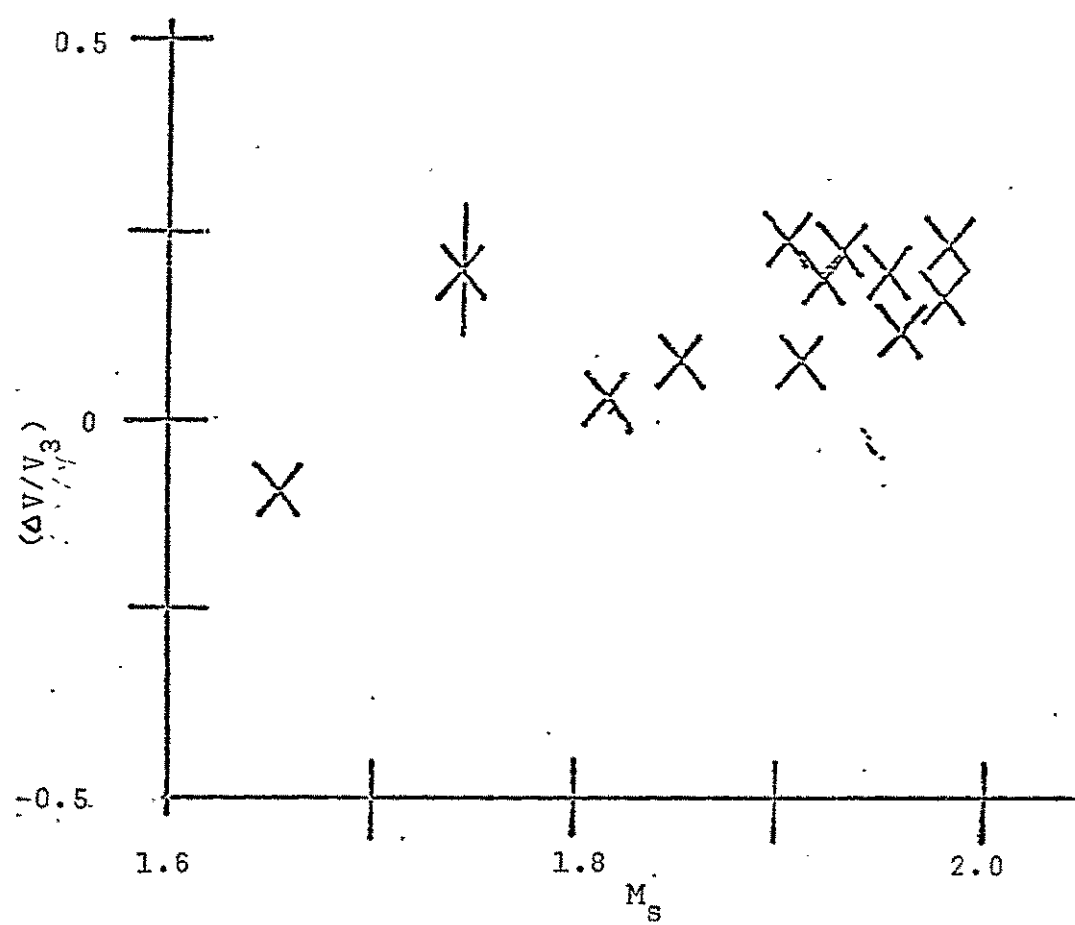


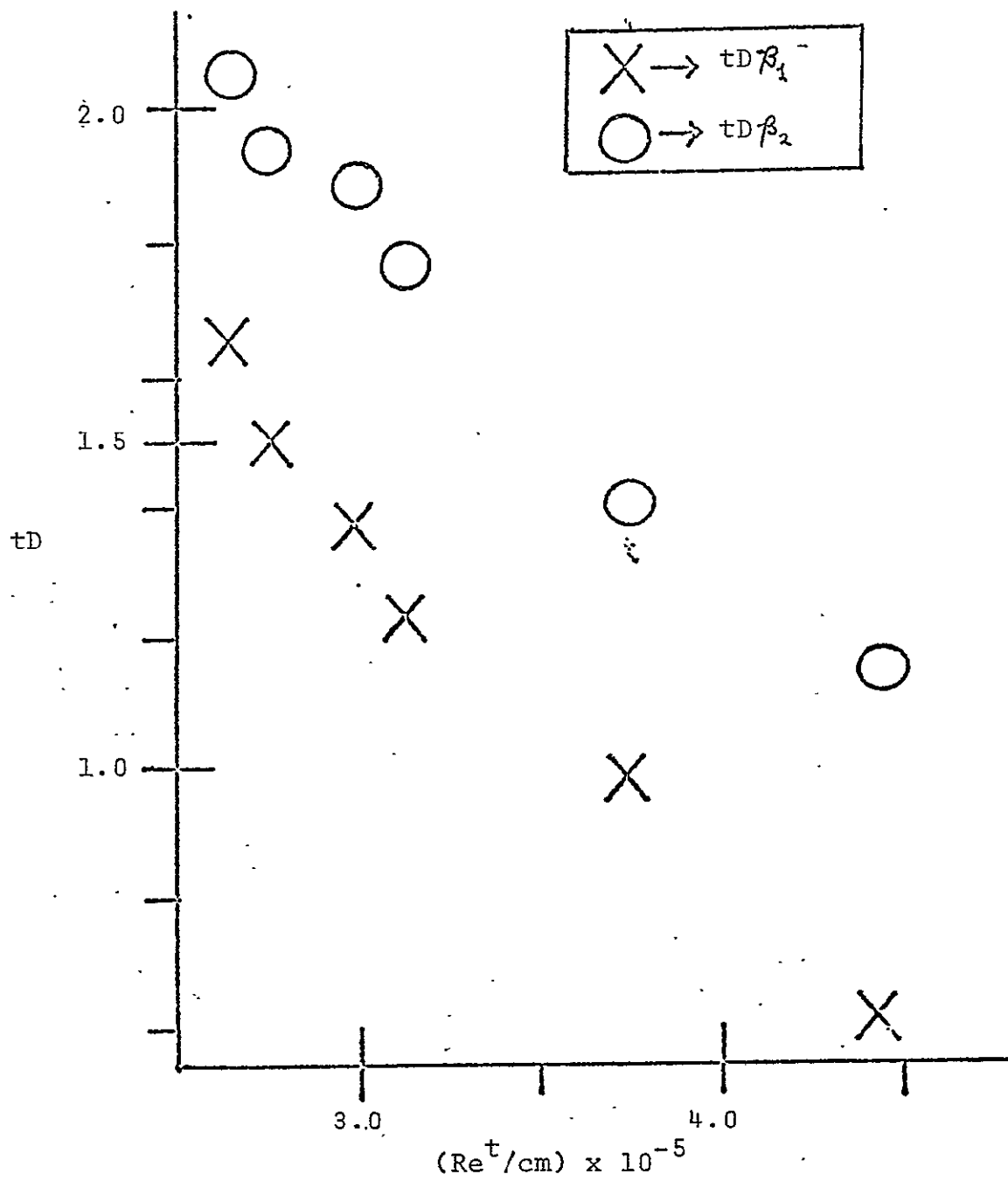




Other dynamical features of the fluctuations have been measured. At a fixed observation station, the width of the deviation in the pressure history  $t_{wp}$  (that is, its duration in the laboratory frame of reference as observed on the oscilloscope trace) appears to be relatively insensitive to increasing time lag  $t_D$  behind the contact surface. This lack of trend is echoed in the duration of the signature for the fluctuation in the interferometer data  $t_{wi}$ . Figure 11a shows this for shock tube firings where simultaneous pressure and interferometer data have been obtained. Figure 11b shows that fluctuations become increasingly less noticeable with time; the magnitudes of the ratio of the peak pressure in the deviation,  $p_B$ , to the local mean pressure  $p_L$ ,  $p_B/p_L$ , diminish with  $t_D^{-1}$ . The speeds of several fluctuations have been measured by tracking them through consecutive pressure stations. When the measured velocities are compared with the local velocity  $v_3$  calculated using the measured primary shock wave's Mach number  $M_s$ , we find that the fluctuations are moving at approximately 90% of the velocity of the local flow ( $\Delta V/V_3 = 0.13 \pm .12$ ). These data are given in Figure 12. Furthermore, we have displayed in Figure 13 a Reynolds number dependence in the time lag behind the contact surface  $t_D$  at which the fluctuations are detected. Shown are those shock tube firings in which two distinguishable fluctuations are discernible in the pressure history. Henceforth, the first fluctuation will be called the  $\beta_1$  fluctuation and the second called  $\beta_2$ . The Reynolds number is based on the local flow conditions calculated for the fully expanded driver gas (region 3) in units of inverse centimeters according to







$Re^t/cm = u_3/v_3$  where  $v$  is the kinematic viscosity. Notice that the separation between the fluctuations seems to be constant for all cases,  $470 \pm 60 \mu\text{sec}$ . Taken separately, the time lag  $t_D$  decreases with increasing  $Re^t/cm$  for both the first ( $\beta_1$ ) and second ( $\beta_2$ ) fluctuations.



## (iii) Boundary Layer Flow Model

Let's model the turbulent contact surface as a boundary layer which is transverse to and symmetric about the axis of propagation. That is, its smallest dimension is at the center of the tube; its largest dimensions (small with respect to the radius of curvature of the front) are at the shock tube's walls. This apparent boundary layer is perpendicular to the "normal" boundary layer at the shock tube's walls. The local Reynolds number in it for the observed fluctuations can be defined using: a local characteristic length,

$$l^* \approx a_3 t_\tau$$

where  $t_\tau$  is a characteristic turbulence time; a characteristic "free stream" transverse boundary layer velocity,

$$U_d = U_3 (\theta^2/8)$$

where  $\nu$  is the total angle subtended by the curved contact surface; and the values of  $\nu_3$  and  $U_3$  computed from the 1-D gasdynamical equations. From Figure 11b, we also assume that the turbulent intensity ( $\approx Q$ ) is related to the time lag of the fluctuations as observed at our test section according to

$$Q \propto P_B/P_L \quad \text{and}$$

$$Q = f_i(i, \dots) (tD\beta_i)^{-1} \quad \text{IV-(1)}$$

In this,  $i$  is a fluctuation ordering parameter and  $f$  is some (unknown) function of  $i$  whose overall value is constant in

our data once the parameter  $i$  is fixed. This assumption does not eliminate the possibility of a  $M_s$  or  $U_3$  dependence; in the data for which the above relationship is confirmed (i.e., the data in Figure 11b), the variation in  $M_s$  was only  $\pm 10\%$ . For consistency, our data require  $f_1 < f_2$  since we find, when  $tD\beta_1 = tD\beta_2$ ,  $(P_B/P_L)_{\beta_1} < (P_B/P_L)_{\beta_2}$ .

In our case,  $t_\tau$  is determined from the correlation functions in our data, as illustrated in Figure 9, to be  $t_\tau \sim 40 \mu\text{sec}$ ;  $\theta$  is estimated from the data reported in Hall<sup>19</sup> and Thompson<sup>24</sup> to be  $\theta = 0.07 \pm 0.02$  rad. The data displayed in Figure 13 ( $tD$  vs  $Re/\text{cm}$ ) is replotted in Figure 14 as  $\log (\frac{1}{tD})$  vs  $Re$  where

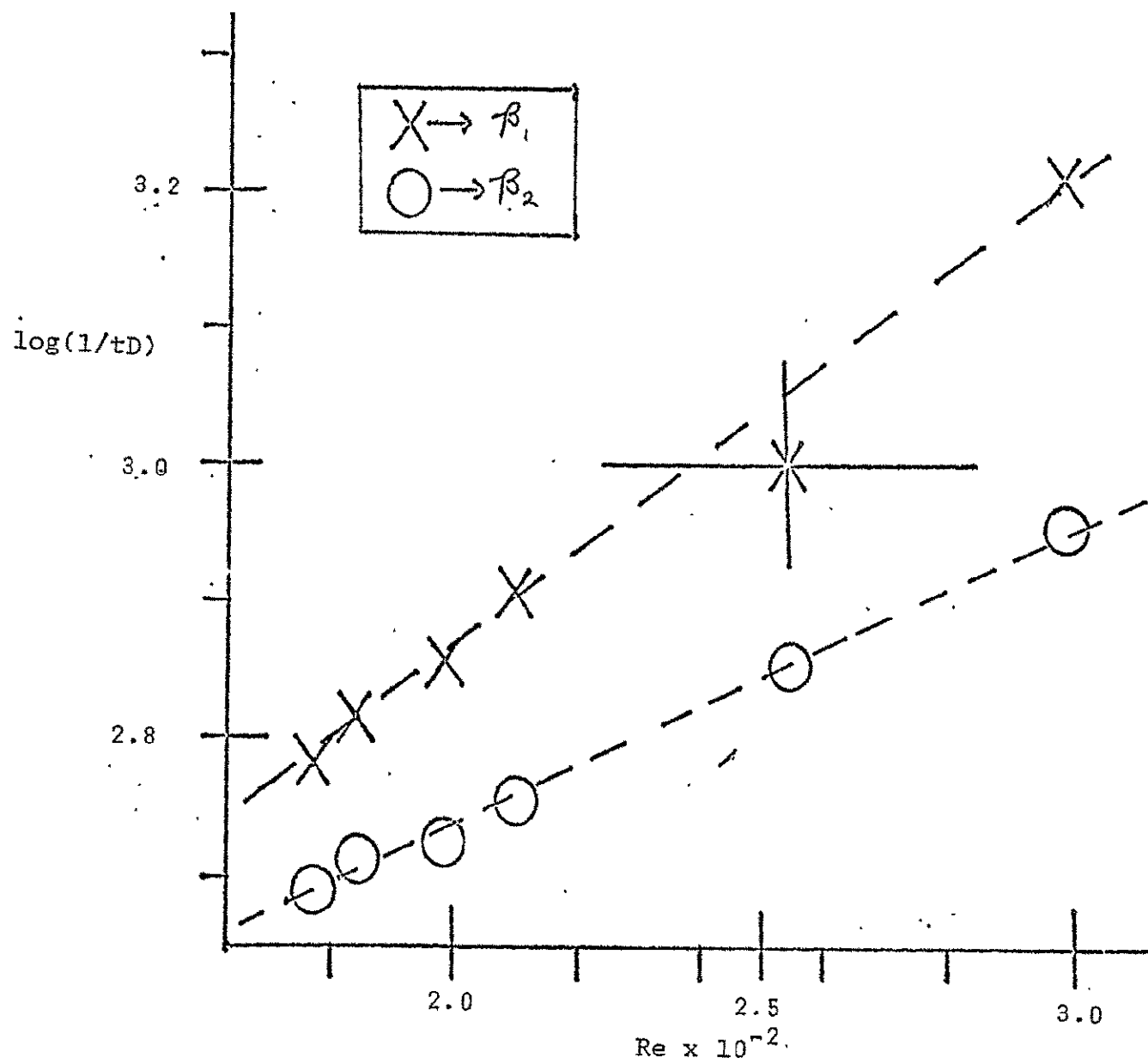
$$Re = \frac{U_3 \theta^2 a_3 t_\tau}{8\nu_3}$$

In both cases, a good fit to a straight line is obtained. For the fit  $\log (1/tD(\beta_i)) = b_i + m_i Re_i$ , we found  $b_1 = -3.8$ ,  $b_2 = -3.7$ ,  $m_1 = 3.3 \times 10^{-3}$ , and  $m_2 = 2.1 \times 10^{-3}$ . Although the correlation coefficient  $r$  is nearly one in both cases, the large uncertainty in  $\theta$  quoted above leaves the fit parameters very uncertain ( $\sim \pm 50\%$ ). Nevertheless, Figure 14 suggests quite clearly a linear dependence of the logarithm of turbulent intensity on local Reynolds.

For transitional boundary layer flow, Tsugé's (1974) solutions dictate the familiar form

$$I \approx Q/Q_0 = \exp [\phi(Re, \lambda)] \quad \text{IV-(2)}$$

The expansion parameter  $\lambda$ , determined by boundary conditions, has the units of frequency;  $Q_0$  is a minimum intensity level which



14.

must be exceeded in order for fluctuations to grow. The function  $\phi$  has no arbitrary constants. The family of curves of  $I'$  vs  $Re$  (where  $I' = \log I$ ) at selected values of the nondimensional ratio  $\lambda v/U_d^2$  shows: a first regime with  $(dI'/dRe) > 0$ ,  $(d^2I'/dRe^2) > 0$ ; a middle regime which is essentially linear, with  $(dI'/dRe) > 0$ ,  $(d^2I'/dRe^2) = 0$ ; and a third regime with  $(dI'/dRe) > 0$  initially and  $(d^2I'/dRe^2) < 0$ . The linear middle regime has a slope which we shall name  $m$  and an intercept on the  $Re$  axis which we name  $Re_n$ . Extrapolated to  $I' = 0$ , the middle regime gives at  $Re = Re_n$ ,  $Q = Q_0$ . The third regime has a maximum in  $I'$  of value  $I'_{mx}$  at a Reynolds number which we now name  $Re_p$ . For the Reynolds number range in Figure 13,  $m = 3 \times 10^{-3}$  and  $(Re_p - Re_n) = (0.56) Re_p - 0.29$ . Since, in the linear regime, the experimental data should fit  $\log Q = b + (m)(Re)$ , the determination of  $Re_n$  gives an estimate of  $Q_0$  from:

$$\log Q \big|_{Re=Re_n} = \log Q_0 = b + (m)(Re_n) \quad IV-(3)$$

Returning to Figure 14, and testing the approach above, one notices that both of the slopes are consistent with the theoretical value within the uncertainty of our estimates. There is no evidence of a peak in the experimental  $Q$  vs  $Re$  profile. However, since Figure 14 tells us that  $Re_p > 310$  if we assume that the theory is applicable, then  $Re_n > 137$  from the discussion above. Combining this inference with equations IV-(1) and IV-(3) and the fit parameters for the  $\beta_1$  fluctuations we find

$$(Q/Q_0) > 4.$$

## E. Conclusion

Our shock tube configuration has provided us access to gasdynamical phenomena not previously reported. From three different diagnostics, viz., pressure measurements, total gas density detection, and reactant density detection, we find localized fluctuations in the gasdynamic variables in the driver gas flow which are distinguishable from the average behaviors. These fluctuations show systematic changes with Reynolds number as well as unique and reproducible features in the nature of their characterizing parameters, viz., time lag with respect to the contact surface, duration, deviation strength, and statistical correlation time. These trends do not allow the interpretation of our fluctuations as a spurious wall boundary layer phenomena. Neither do these trends seem affected by the variety of diaphragm materials and diaphragm rupturing procedures used. However, the trends are not inconsistent with an interpretation of the observed fluctuations as examples of turbulent bursts, originating in an unstable contact surface. In addition, attempting to interpret the contact surface as a boundary layer in accordance with Tsugé's kinetic theory of turbulence, we find a qualitative success in terms of the Reynolds number trend with turbulent intensity. We can compare the form taken by our data with the form taken by theoretical solutions in the same Reynolds number range and estimate that the ratio of required maximum to minimum turbulent fluctuation level for amplifiable instabilities must be at

least four. This overall approach should therefore be extended to and tested on a wider class of unstable gasdynamic discontinuities.

## V. Improving the Mach Number Capabilities of Arc Driven Shock Tubes.

### A. Introduction

25

The pressure loaded arc driven shock tube has proven to be an invaluable tool in the study of high speed, high temperature fluid phenomena and in the creation of high temperature plasmas. The continuing need for improved overall effectiveness for such devices has motivated a lot of work on the effects of circuit inductance, capacitance, impedance matching and driver tube configuration on the efficiency of conversion from electrical energy to test gas kinetic energy. 25-29 The upper limit of Mach numbers attainable from shock tubes has correspondingly increased. However, insofar as systematic trends in performance estimators are concerned, these previous results have seemed to be either tentative or inconclusive.

We, therefore, have analyzed the scaling of shock tube performance with capacitor energy, initial driver gas pressure and driver volume. We have used data published in the literature from ambitious and large configurations as well as the measurements from our own modest facility. Specifically, we have chosen to try to learn as much as possible from the simplest model of the shock wave pressurizing process. With this kind of device, we expect to ultimately produce the well-known collisional turbulent shock fronts arising from electron recombination processes. Section VI gives background for our planned extensions of current diagnostic techniques for application to the shock tube environment.

## B. The Pressurization Process

In general, pressure loaded arc driven shock tubes can be thought of as operating in the same way as ordinary pressure driven shock tubes. The electric arc resulting from a spark discharge between two electrodes heats up the driver gas, uniformly increasing its pressure and temperature at constant volume. The increased pressure and driver gas speed of sound should routinely allow greater Mach numbers to be obtained in the driven tube test gas after bursting a diaphragm separating the two sections than would otherwise be obtained without preheating. We shall assume that this model adequately characterizes the pressure loaded arc driven shock tube.

The performance of the shock tube is often discussed in terms of the highest Mach numbers which it might provide. However, the speed of the shock wave obviously depends on both the driver and driven gas parameters. Therefore, one should not expect to successfully use the Mach number alone when comparing the performance of different shock tubes if there are varying configurations and operating conditions.

A more useful basis for comparison can be found as follows.  
 Recall, <sup>30</sup> for a strong shock wave, that the Mach number is expressed as

$$M = \frac{\gamma_1 + 1}{2} \left( \frac{\gamma_4 T_4 \mu_1}{\gamma_1 T_1 \mu_4} \right)^{1/2} \frac{u}{c_4} \quad V-(1)$$

where  $u/c_4$  is an implicit solution of the equation

$$\frac{u}{c_4} = \frac{2}{\gamma_4 - 1} \left[ 1 - \left\{ \frac{\gamma_4 (\gamma_1 + 1)}{2} \frac{\rho_1}{\rho_4} \left( \frac{u}{c_4} \right)^2 \right\}^{(\gamma_4 - 1)/2\gamma_4} \right] \quad V-(2)$$



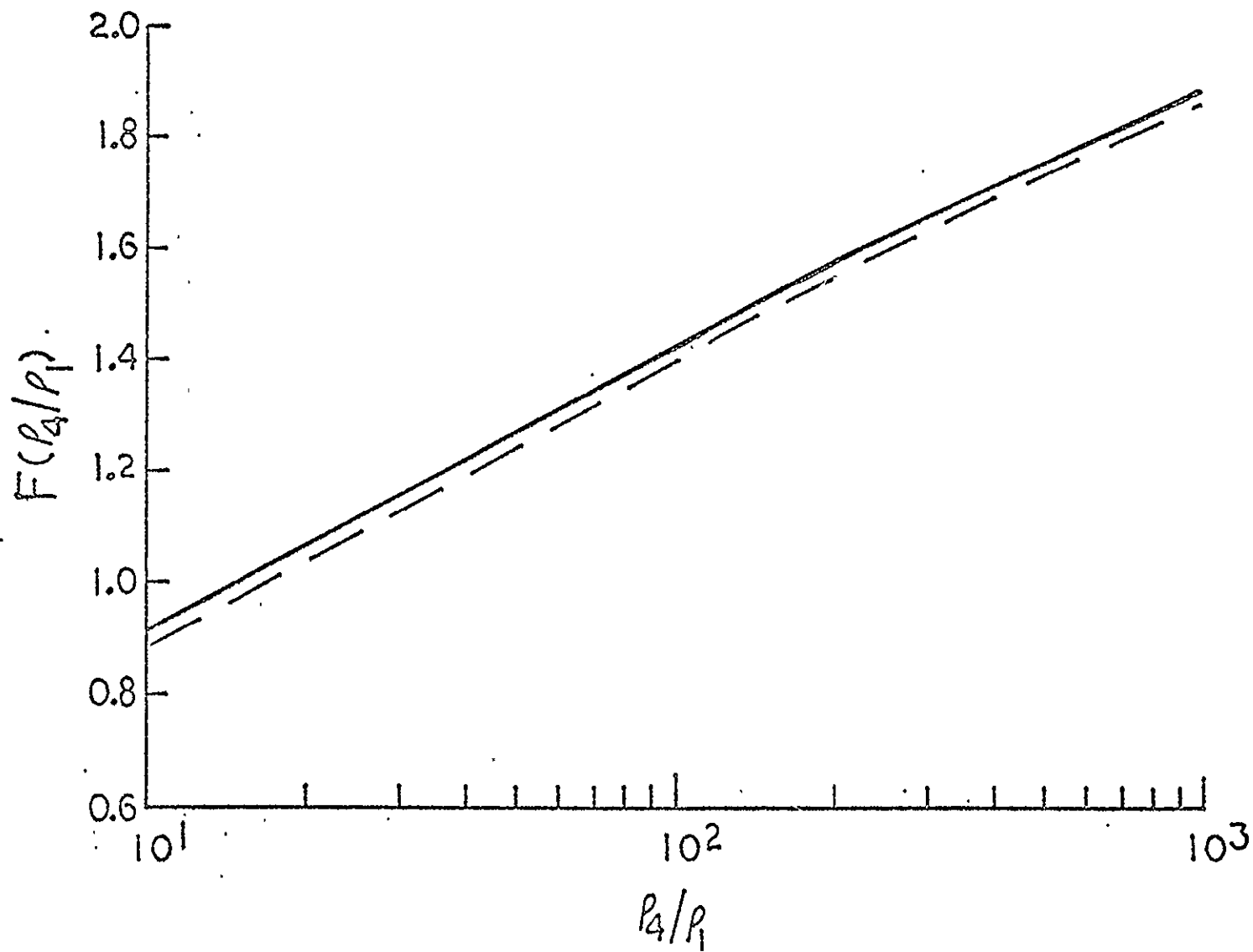
Here, using conventional notation,  $\gamma$  is the ratio of specific heats,  $T$  is the temperature,  $\mu$  the molecular weight,  $\rho$  the gas density,  $u$  is the gas flow velocity and  $c$  is the speed of sound. When this formulation is applied to our model, the subscript 1 refers to the quiescent driven gas and the subscript 4 refers to the driver gas after the discharge but before the rupture of the diaphragm.

The solution of Equation V-(2),  $u/c_4 = F(\rho_4/\rho_1)$ , can be obtained numerically. Figure 15 shows solutions for two sets of  $\gamma$ 's. We note that  $F(\rho_4/\rho_1)$  is not a very strong function of  $\rho_4/\rho_1$ . The more important parameter for increased Mach number is, therefore,  $T_4$ , which depends only on driver gas conditions.

It is well known that the cost of a shock tube facility is usually a very sensitive function of the cost of capacitors and related power supplies, i.e., on  $E_c = (1/2)CV_c^2$ , the energy available to the driver gas. Thus we have chosen, as a result of these considerations, to use the ratio of stored capacitor energy  $E_c$  to shock heated driver gas temperature  $T_4$ :

$$\eta \equiv \frac{E_c}{T_4} \text{ Joules/}^\circ\text{K} \quad \text{V-(3)}$$

as our measure for comparison. The  $\eta$  is an index of performance loss since an improvement in energy transfer to the driver gas shows up as a reduction in  $\eta$ .



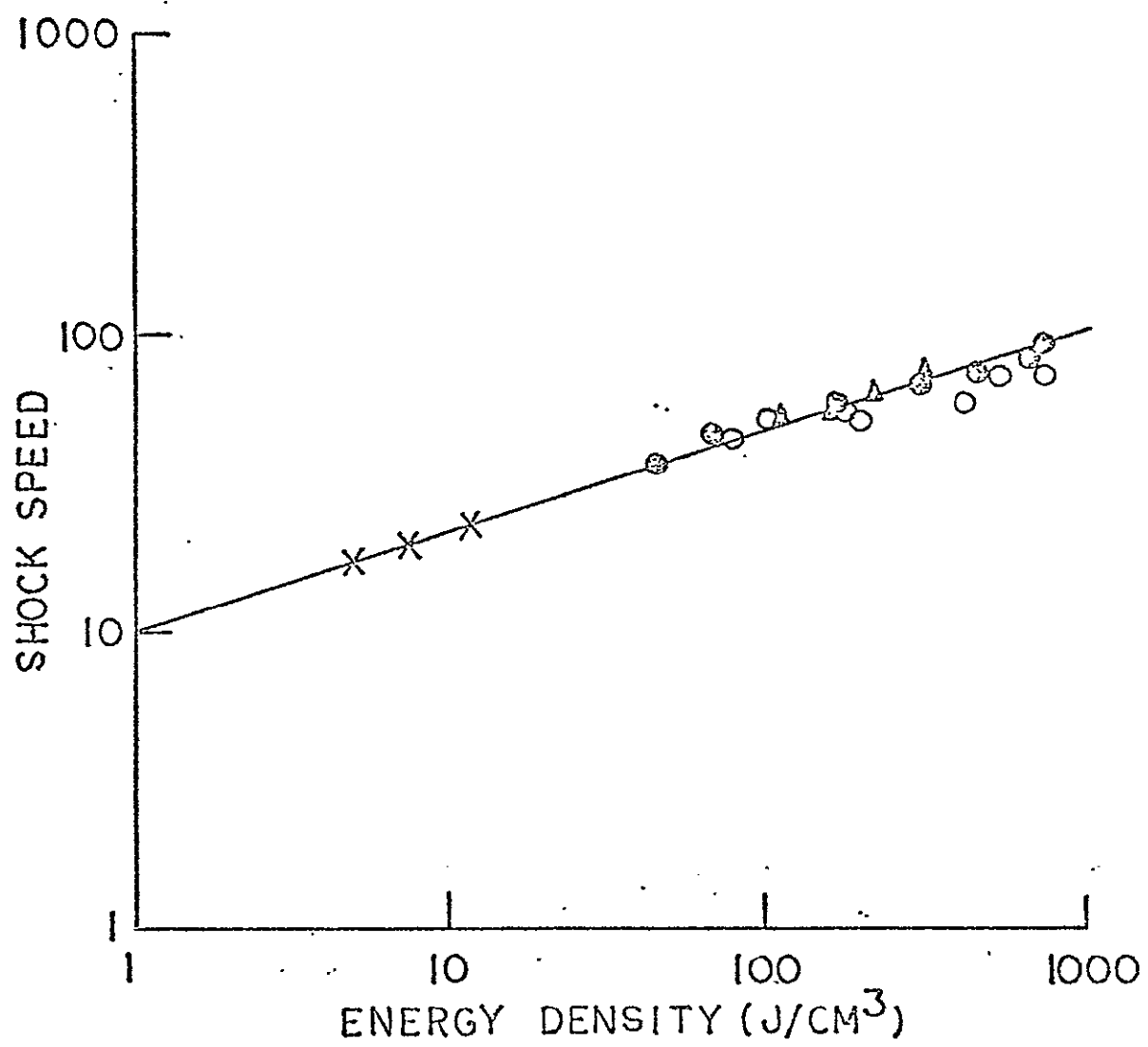
### C. Performance Analyses

The most interesting configurations for these arc driven shock tubes have been either those with cylindrical drivers with exploding wire triggers or those with conical inserts in the driver tubes.<sup>29</sup> To us, the range of data available seemed deficient in the low energy and small driver gas volume regime. Our configuration has been chosen so as to begin to remedy this deficiency.

In our set-up, we have used a cylindrical driver (with electrodes similar to that of the conical driver), 10 cm long with a diameter of 5 cm. Arc heating results when a 12  $\mu\text{F}$  capacitor charged to 20 kV is discharged through a spark gap in the driver tube to which the capacitor is coupled by a parallel plate transmission line. The luminous shock front is monitored using piezoelectric pressure transducers, photomultipliers and the usual associated diagnostic electronics. Helium and argon were used as the driver and driven gases respectively.

#### (i) Dependence on $E_c$ and $V_4$

The dependence of the shock speed on driver energy density has been computed for several facilities. The results are given in Figure 16. The speed shown there is in arbitrary units. Each set of data has been multiplied by a constant uniquely determined for that set; the constant was determined so that all of the data would fall near a single line for the purpose of looking



for a simple overall secular trend. It is quite evident that such a trend exists; the speed scales as  $(E_c/V_4)^{1/3}$ , the cube root of the ratio of stored capacitor energy to driver volume. Since  $M^2 \sim T_4$  and  $T_4 = E_c/\eta$ , Figure 16 tells us that

$$\eta \sim E_c^{1/3} V_4^{2/3} \quad V-(4)$$

This scaling of  $M$  with  $E_c$  may be due to increased losses at higher currents and to reduced discharge resistance at high temperature (current). The cost per unit temperature increase of driver gas increases with  $E_c$ . Notice that there is no sign of a levelling off of speed with increasing  $E_c$  even at the highest energies. Thus, it may be that the speed one obtains depends only on one's willingness to invest in bigger capacitor banks.

Figure 16 also suggests decreasing  $V_4$  as a way of increasing performance without increasing the cost. Of course, this would be achieved at the risk of reduced time available for experimental measurements at a fixed test station location.

An unadjusted numerical comparison of some of the overlapping data is given in Table I. At comparable Mach numbers, one sees that increased  $V_4$  is associated with increased  $\eta$ . Our driver, as would be expected, has approximately the same performance as a conical tube if a scaling of our results to the higher energies is performed.

(ii) Dependence on Initial Driver Gas Pressure  $p_{4i}$

For a partially ionized plasma discharge column, the resistivity will increase with increasing gas pressure. Increasing the resistance of the gap will increase the energy dissipated in the arc. A higher pressure, on the other hand, will mean a greater mass of driver gas, a larger driver gas heat capacity, i.e., a reduced  $T_4$ , and therefore an increased index of performance loss  $\eta$ .

We have measured the dependence of Mach number  $M$  on  $p_{4i}$ . The results are shown in Figure 17. Note the existence of a plateau at high pressure where  $M$  becomes effectively independent of  $p_{4i}$ . Since  $T_1 = T_{4i}$  in our set up then  $p_{4i} = RT_{4i} = RT_1$ . The fractional efficiency of electrical energy conversion is given by

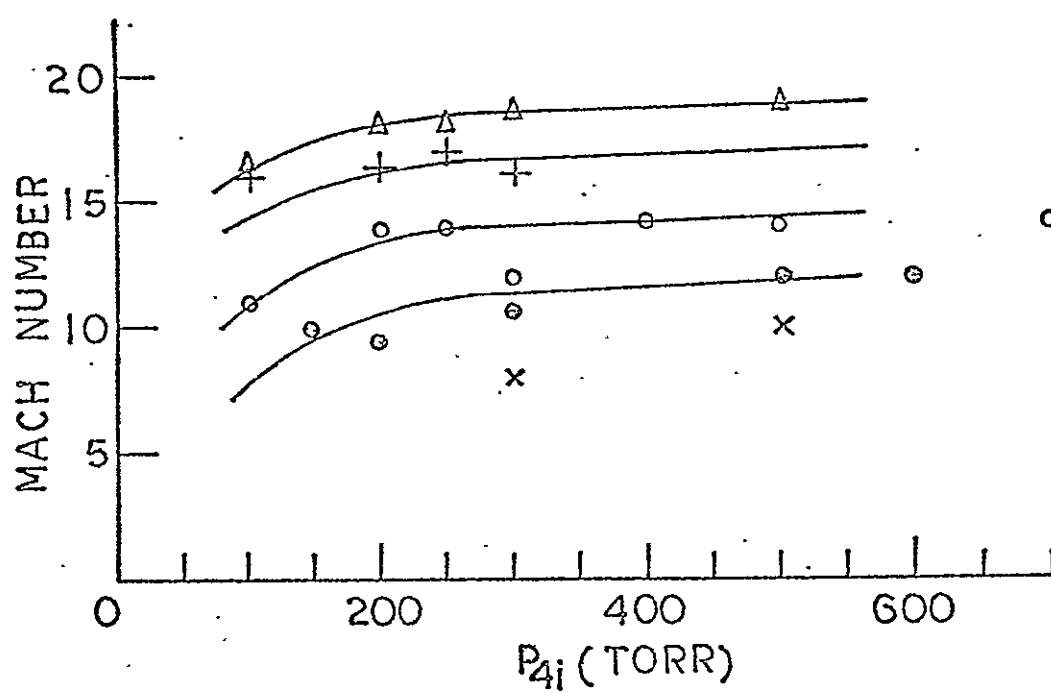
$$\epsilon = \frac{3}{2} \rho_4 RT_4 / (E_c / V_4)$$

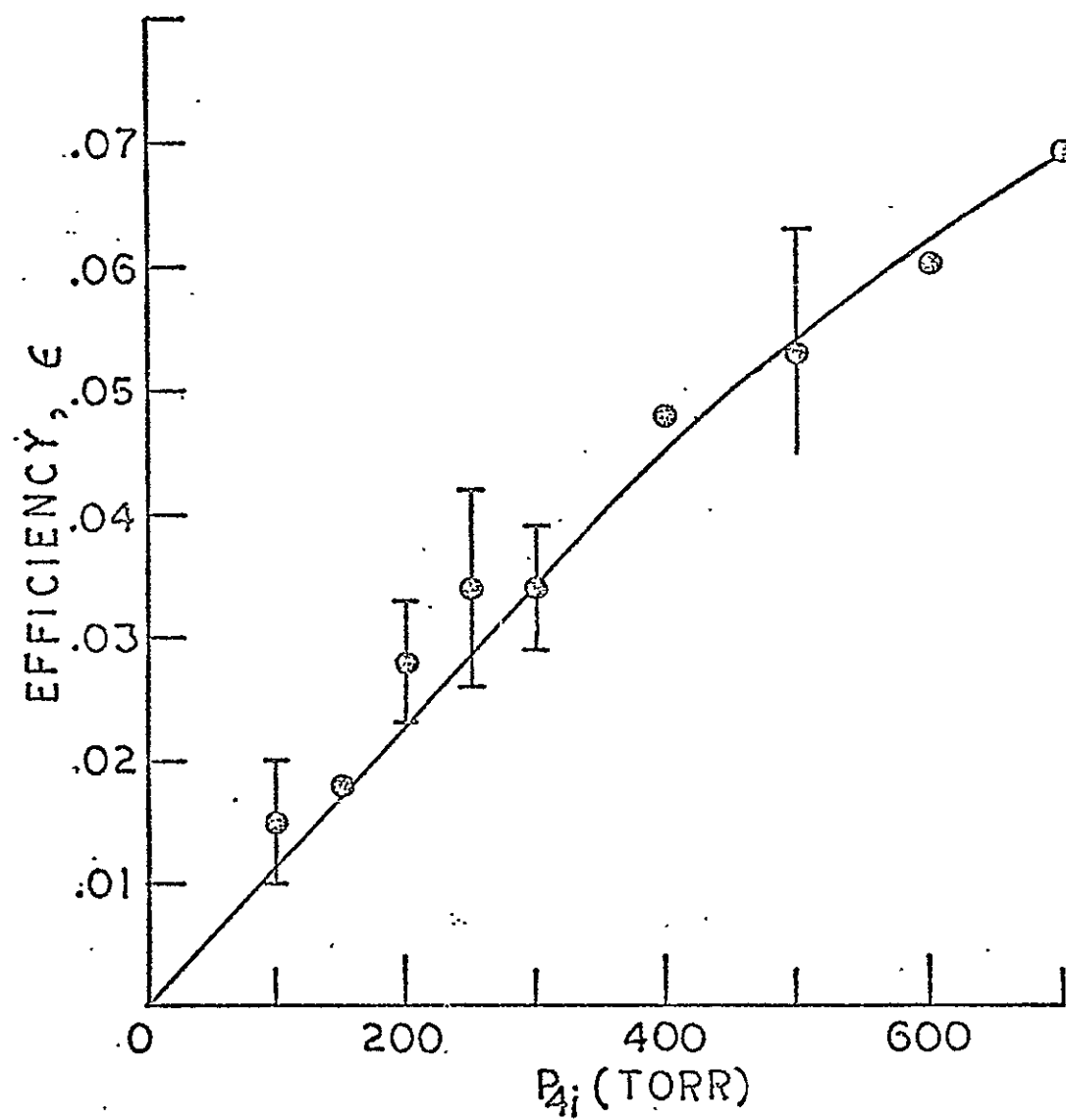
and we find, using equation V-(1),

$$M \sim \left( \frac{\epsilon}{p_{4i}} \right)^{1/2} F(\rho_4 / \rho_1)$$

Thus, the plateau in Figure 17 implies that the resistivity does not increase with pressure fast enough to compensate for the increased heat capacity of the driver gas.

This inference is confirmed in Figure 18. The measured efficiency is explicitly shown to have a dependence on  $p_{4i}$  which is too weak for an increase in  $p_{4i}$  to be reliably impactful on the Mach number.







Thus, it seems unnecessary to operate the pressure loaded arc driven shock tube at the ultra high driver pressures which are now often used unless there is some motivation other than improved performance. Reduced driver pressure, wherever possible, will eliminate the need for heavy and expensive driver tube designs. The lower limit for  $p_{4i}$  should be determined, insofar as these analyses are concerned, by the need for reproducible flow properties.

(iii) Dependence on Discharge Length

The total resistance of a discharge is directly proportional to its length. For maximum energy dissipation in the arc, the length of the arc should be maximized for a given driver volume. Using the efficiency as defined above,

$$T_4/T_1 = 1 + \left(\frac{2}{3} \epsilon E_c / V_4\right) / (\rho_4 R T_1) .$$

At large Mach numbers,

$$T_4/T_1 = (2 E_c) / (3 V_4 \rho_4 R T_1) = E_c / \eta T .$$

Hence

$$\epsilon = (3 V_4 \rho_4 R / 2 \eta) \sim \left(\frac{E_c}{V_4}\right)^{-1/3} \quad V-(5)$$

and we see that the efficiency of conversion increases with increasing discharge length ( $\sim V_4^{1/3}$ ).

Nonetheless, increasing  $V_4$  to increase resistance and conversion efficiency is not advisable since it decreases the total energy density and increases the index of performance

loss  $\eta$  as discussed above. Attempts, therefore, to improve performance through the management of driver gas circuit resistance inevitably encounter a fundamental handicap.

#### D. Conclusions

A simple physical model of shock wave pressurization has apparently succeeded in providing a consistent overall interpretation of the performance of a variety of pressure loaded arc driven shock tubes. This model should be limited only in the sense that the equations of one-dimensional gas dynamics are usually limited in shock tube analyses.<sup>30</sup> Within these limits: The change in electrical conversion efficiency resulting from a change in the initial driver gas pressure does not significantly improve either the performance or the highest Mach number available from a given facility once a nominal operating  $p_{4i}$  has been ascertained. Secondly, increasing the discharge volume so as to increase the conversion efficiency represents a change in configuration in this model. Table I, equation V-(4) and equation V-(5) show that such a change can be expected to have a complicated effect on the index of performance loss (and cost) and Mach number; the driver volume should be the smallest compatible with experiment test times and the discharge length should be maximized for this volume. However, at constant volume, Mach numbers and the index of performance loss can be expected to increase (while the efficiency decreases) indefinitely with the cube root of capacitor energy.

TABLE I

| TYPE  | $E_C$  | $p_{4i}$              | $V_4$ (cm <sup>3</sup> ) | M  | $T_4/T_1$ | $p_1$<br>air | $\eta$               | Ref. |
|---|--------|-----------------------|--------------------------|----|-----------|--------------|----------------------|------|
| cylindrical driver;<br>spiral trigger wire                | 1 MJ   | 27.2 atm<br>He        | 5969                     | 44 | 44        | 1 Torr       | 7 MJ/K               | 1    |
|   |        |                       |                          | 34 | 41        | 10 Torr      |                      |      |
|   |        |                       |                          | 22 | 37        | 100 Torr     |                      |      |
| cylindrical driver;<br>straight trigger<br>wire           | 1 MJ   | 27.2 atm<br>He        | 5969                     | 30 | 21        | 1 Torr       | 15 MJ/K              | 1    |
|   |        |                       |                          | 23 | 19        | 10 Torr      |                      |      |
|   |        |                       |                          | 16 | 20        | 100 Torr     |                      |      |
| conical driver  | 235 kJ | 9.2 atm<br>He         | 632                      | 55 | 57        | 0.1 Torr     | 1.4 MJ/K             | 2    |
|   |        |                       |                          | 39 | 42        | 1 Torr       |                      |      |
| conical driver  | 290 kJ | 11.8 atm<br>He        | 350                      | 85 | 132       | 0.05 Torr    | 0.7 MJ/K<br>1.3 MJ/K | 3    |
|   |        |                       |                          | 80 | 68        | 0.05 Torr*   |                      |      |
| Present work<br>cylindrical driver<br>spark gap triggered | 2.4 kJ | less than<br>1 atm He | 203                      | 14 | 8         | 1 Torr*      | 0.09 MJ/K            | -    |
|   |        |                       |                          | 19 | 8         | 0.1 Torr*    |                      |      |

\* Driven gas is argon.

## VI. Resonant Absorption in an Argon Plasma at Thermal Equilibrium

### A. Introduction

The absorption of resonant argon ion laser radiation has been proposed as a sensitive temperature diagnostic for an argon plasma in thermal equilibrium.<sup>32</sup> Absorption as a diagnostic for electron density and temperature is a well established technique in plasma physics that supplements other well known techniques such as line and continuum intensity measurements, probe measurements, light scattering, interferometry, and so on. The main advantage of absorption is in its relative simplicity; all that is needed is a light source (laser) and a detector without the need for calibration. On the other hand, absorption coefficients depend on both the density and the temperature and, their use has the disadvantage of requiring an independent measurement of one of these parameters. The calculation of the absorption coefficient in Ref. 32 has two noteworthy features: (1) the absorptions due to free-free transitions (inverse bremsstrahlung) and bound-free transitions (photo-ionization) are neglected; (2) the effects of Doppler broadening at low densities and high temperatures are not included. In this paper, we present calculations of the absorption coefficient of an equilibrium argon plasma at  $\lambda = 4880 \text{ \AA}$  without the limitations just mentioned and evaluate their implications.

## B. Theoretical Approach

### (i) The Absorption Coefficient

The total absorption coefficient  $K$  can be expressed as

$$K = (1 - (v_p^2/v^2))^{-\frac{1}{2}} (K_{ei} + K_{en} + K_p + K_r) \quad \text{VI-(1)}$$

where  $v_p$  is the plasma frequency and  $v$  is the laser frequency. The contributions to  $K$  indicated in equation VI-(1) come from the following contributions: (i) electron inverse bremsstrahlung in the presence of an ion,  $K_{ei}$ ; (ii) inverse bremsstrahlung by electrons during collisions with neutral atoms,  $K_{en}$ ; (iii) photo-ionization of highly excited atoms and ions,  $K_p$ ; (iv) resonance absorption of 4880 Å radiation by Ar II ions,  $K_r$ . Let's now explicitly characterize these contributions.

The absorption coefficient due to electron inverse bremsstrahlung in the field of ions is:

$$K_{ei} = \frac{3.692 \times 10^8 n_e}{v^3 T^{1/2}} (n_{11} + 4n_2 G_2) \quad (\text{c.g.s.}) \quad \text{VI-(2)}$$

where  $n_e$ ,  $n_1$ , and  $n_2$  are the electron, singly charged ion and doubly charged ion densities respectively,  $T$  is the temperature and  $G_1$  and  $G_2$  are the Gaunt factors. The value of  $G_1$  is taken from Schnapauff's work<sup>34</sup> ( $G_1 = 1.7$ ) and  $G_2$  is assumed to be equal to one; the Gaunt factors are relatively insensitive to the temperature.

The electron-neutral atom inverse bremsstrahlung absorption

coefficient can be approximated by the expression used in  
microwave theory:

$$K_{en} = \left( \frac{e^2 n_e}{\pi m_e c} \right) v_{eff} \left\{ v^2 + \left( \frac{v_{eff}}{2} \right)^2 \right\}^{-1} \quad \text{VI-(3)}$$

where  $v_{eff} = n_o \langle v \sigma_{tr} \rangle$ . Here,  $n_o$  is the density of neutrals and  $\langle v \sigma_{tr} \rangle$  is the product of the electron velocity and the cross-section for momentum transfer collisions averaged over a Maxwellian distribution. The value of  $\sigma_{tr}$  used in the calculation is taken from Engelhardt and Phelps.<sup>36</sup> The validity of using equation VI-(3) in the visible wavelengths is discussed in numerous papers dealing with laser induced gas breakdown.<sup>37</sup> We notice in passing that the electron inverse bremsstrahlung absorption during collisions with neutrals is generally much smaller than the electron inverse bremsstrahlung except when the degree of ionization is less than 1%.

The contribution of photoionization of highly excited atoms is:

$$K_p = \frac{2C_1 T}{v^3} \left\{ \frac{n_o g_1^O}{U_o} \exp \left( - \frac{(\chi_1 - \Delta \chi_1)}{KT} \right) \xi_1 + \frac{4g_2^O n_1}{U_1} \right. \\ \left. \times \exp \left( - \frac{(\chi_2 - \Delta \chi_2)}{KT} \right) \xi_2 \right\} \left\{ \exp \left( \frac{h\nu}{KT} \right) - 1 \right\}, \quad \text{VI-(4)}$$

$$C_1 = \frac{16\pi^2 k e^6}{3\sqrt{3} Ch^4} = 8.915 \times 10^{23} \quad (\text{c.g.s.})$$

where  $g_1^O$  and  $g_2^O$  are the statistical weights of the ground states of the first and second ionization stages respectively and  $U_0$  and  $U_1$  are the partition functions of Ar I and Ar II with ionization potentials  $\chi_1$  and  $\chi_2$ . The lowering of the ionization potentials due to the plasma charges are  $\Delta\chi_1$  and  $\Delta\chi_2$ . The factors are essentially independent of temperature in the visible region of the spectrum. The values for  $\xi_1$  obtained by Schlüter<sup>38</sup> and the values of  $\xi_2$  as measured by Vorpaeva<sup>39</sup> are used in our calculations.

The absorption coefficient of radiation in resonance with this transition is

$$K_r = \frac{h\nu}{c} B_{lu} \phi(\nu) \left( n_l - \frac{g_l n_u}{g_u} \right) = \frac{h\nu}{c} B_{lu} \phi(\nu) n_l (1 - \exp(-h\nu/KT)) \quad \text{VI-(5)}$$

where  $B_{lu}$  is the Einstein B coefficient and  $\phi(\nu)$  is the absorption lineshape. In this, we define  $n_l$ ,  $n_u$  and  $g$ ,  $g_u$  as the densities and statistical weights of singly charged ions in the lower ( $4s^2P_{3/2}$ ) and upper ( $4p^2D_{5/2}$ ) levels of the 4880 Å argon ion transition, i.e.,

$$n_l = \frac{g_l}{U_1} n_1 \exp(-E_l/KT), \quad n_u = \frac{g_u}{U_1} n_1 \exp(-E_u/KT). \quad \text{VI-(6)}$$

The reduction in absorption due to stimulated emission is incorporated in equation VI-(5) and the laser linewidth is assumed to be much smaller than the absorption linewidth.

The lineshape factor  $\phi(\nu)$  is a convolution of the (Gaussian or) Doppler and Stark broadened lineshapes. Doppler broadening will dominate in the low density, high temperature case while Stark

broadening will dominate at high densities. A large fraction of the total Stark broadening will be due to electron impacts which produce a Lorentzian lineshape about a central frequency,  $\nu_0$ :

$$\phi_s(\nu) = \frac{(\Delta\nu_s/2\pi)}{(\nu-\nu_0)^2 + (\Delta\nu_s/2)^2} \quad \text{VI-(7)}$$

where  $\Delta\nu_s$  is the full width at half intensity maximum.

In addition to Stark broadening, there is a Stark shift of the line center, so that  $\nu_0$  and the laser frequency  $\nu_L$  do not coincide, of magnitude  $d$  where

$$\nu_0 = \nu_L + d \quad \text{VI-(8)}$$

Neglecting ion broadening,  $\Delta\nu_s$  and  $d$  will be proportional to  $n_e$  and are weak functions of the temperature. (The validity of the above assumptions concerning Stark effects and the errors involved therein are fully discussed in Ref. 32.) The linewidth and the Stark shift parameters for the 4880 Å transition are taken from the measurements by Labat.<sup>40</sup>

At very high electron densities, other Ar I and Ar II lines may be sufficiently broadened and shifted so as to contribute to the absorption. However, since this only occurs when the bremsstrahlung and photoionization dominate, resonance absorption at the far wings of other lines is not included in our calculations given below.



## (iii) Plasma Composition

For a fixed electron or gas density, the plasma composition is computed using the Saha equation and the laws of conservation of mass and charge. We satisfy conditions for local thermodynamic equilibrium as discussed by Griem.<sup>41</sup> The lowering of the ionization potentials is determined from the Debye-Hückel theory.<sup>35</sup>

$$\Delta\chi_m = \frac{me^2}{\lambda_0} \quad \text{VI-(9)}$$

The partition functions are computed by summing over the energy levels tabulated by Moore<sup>42</sup> and integrating over assumed hydrogenic levels for the excited states close to the continuum. The same ionization potential lowering is assumed in the calculation of the partition functions and in the Saha equation. Plasma composition is computed through the first, second, and third ionization stages (i.e., for  $n_1$ ,  $n_2$ , and  $n_3$ ).

## (iii) Limitations of Theory

The limits on the laser power to be used,  $W$ , have been discussed in Ref. 32. The lower limit is determined by the ratio of the transmitted laser power to the spontaneous emission. The upper limit is determined by the condition that the absorption of laser energy should not appreciably perturb the system. The result in Ref. 32 is:

$$2 \times 10^{-21} n_e \leq W \leq 4 \times 10^{-32} n_e^2$$

for a beam diameter of 2 mm and a beam divergence of  $10^{-5}$  sterad.

The criterion for the existence of LTE has been formulated

by Griem. To insure collisional domination up to the ground state, the radiative population rate of the ion ground state from the resonance level should be 10 times smaller than the corresponding collisional population rate. This translates to

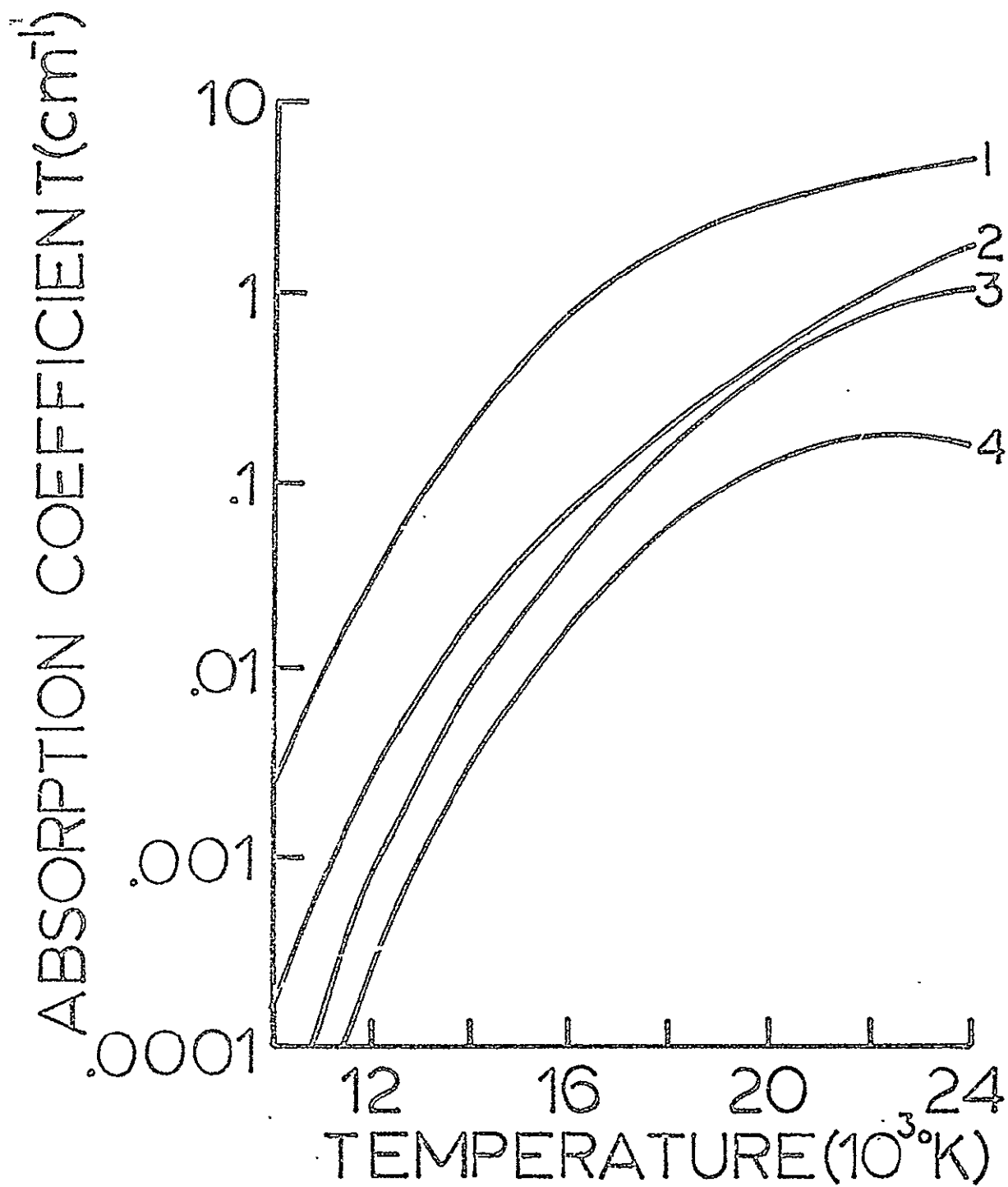
$$n_e \geq 2 \times 10^{13} T^{1/2} \text{ cm}^{-3}.$$

Furthermore, calculations based on a collisional radiative model<sup>12</sup> indicate that at  $n_e = 10^{16} \text{ cm}^{-3}$  LTE exists for the Ar I and II systems at an electron temperature of  $T_e = 4 \text{ eV}$ . Since the lower the temperature the easier LTE is reached, then LTE is assured when  $n_e \geq 10^{16} \text{ cm}^{-3}$  and  $T_e \leq 25,000 \text{ K}$ .

The assumption of Stark broadening by electron collisions only entails an error of about 8% for  $10^{16} \leq n_e \leq 10^{21} \text{ cm}^{-3}$  and  $10,000 \leq T \leq 40,000 \text{ K}$ .<sup>32</sup> Finally, the assumption of a very narrow laser line compared to the Stark broadened absorption line is easy to satisfy with commercial argon ion lasers especially if one uses a single mode laser.

C. Applications:  $10^{16} \text{ cm}^{-3} < n < 10^{19} \text{ cm}^{-3}$ ;  $10^4 \text{ }^\circ\text{K} < T < 2.4(10^4) \text{ }^\circ\text{K}$

Using equation VI-(1), the absorption coefficient  $K$  is first computed as a function of temperature at fixed gas densities  $n (=n_0 + n_1 + n_2 + n_3)$ . The results are shown in Figure 19. For a fixed  $n$ , we see that absorption is sensitive to temperature. However, for  $n \lesssim 10^{17} \text{ cm}^{-3}$ , the absorption coefficient is not a single valued function of the temperature. This is due to a shift in the balance between the free-free and bound-free transitions' contributions to the absorption coefficient (which decrease with increasing temperature) and the contribution from



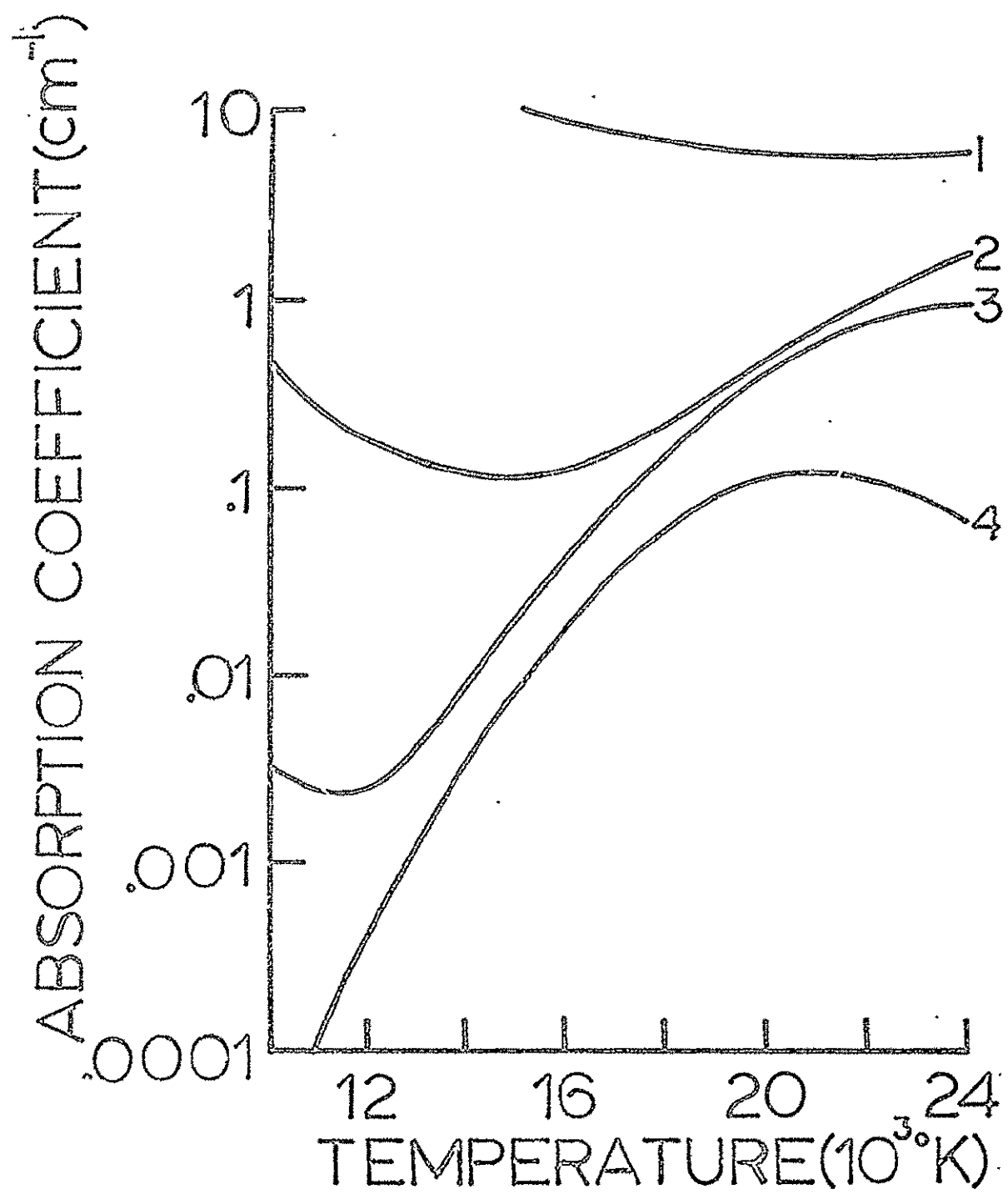
resonance absorption (which increases with increasing temperature).

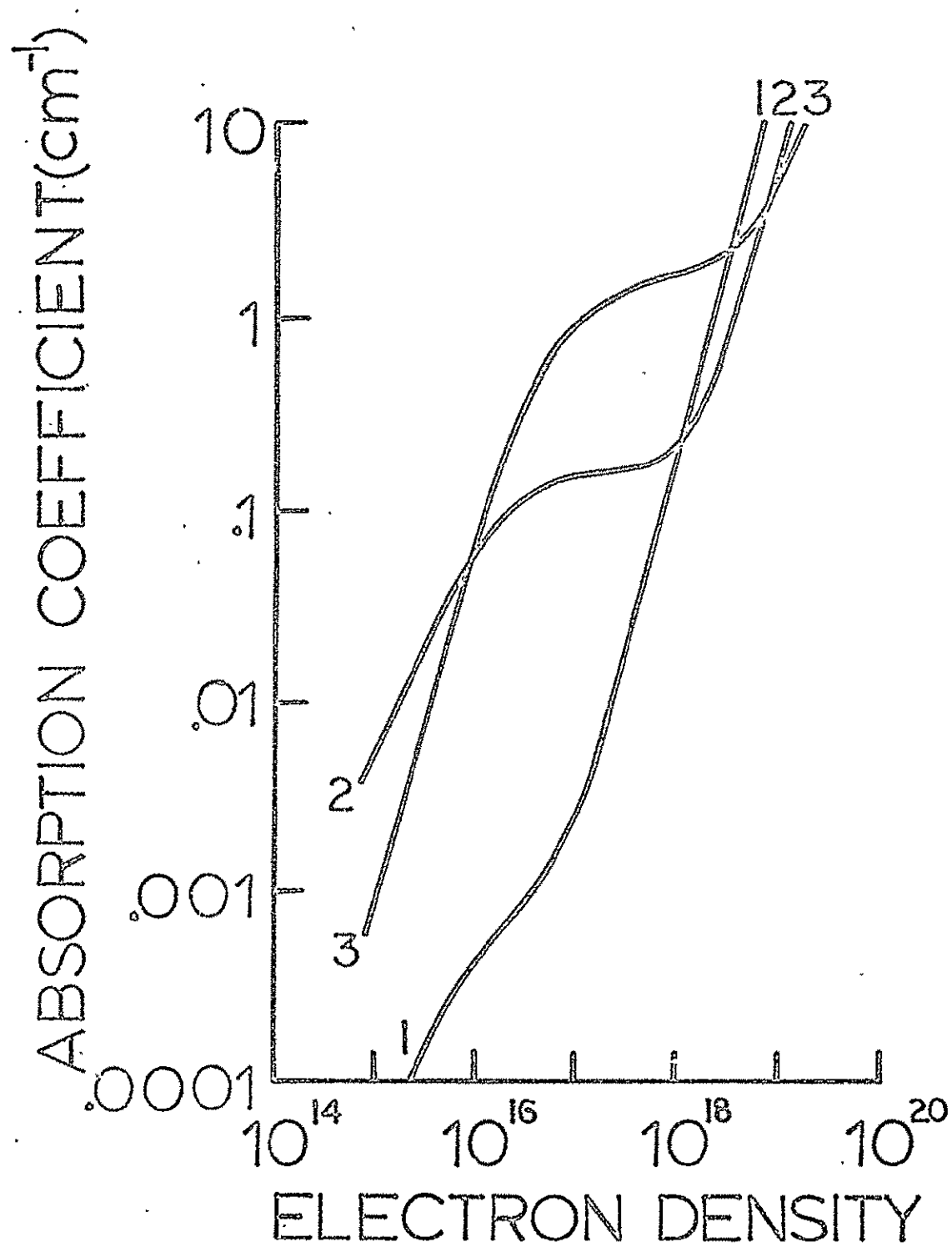
Figure 20 shows our results when the absorption coefficient is computed as a function of temperature at fixed electron densities. Except at very low electron densities (where the validity of an LTE assumption becomes marginal), the absorption coefficient is not very sensitive to temperature in this case. In addition, the absorption coefficient is a multi-valued function of temperature throughout the computed range. This result is markedly different from those in Ref. 32 where no dependence of the absorption coefficient on electron density was obtained.

We, therefore, also calculated the dependence of the absorption coefficient on the electron density at fixed temperatures. Here,  $K$  is very sensitive to temperature. However, the behavior becomes complicated, with increasing temperature, by a plateau regime in which a large change in the electron density can leave the absorption coefficient relatively unaffected. (See Figure 21.) Notice that the dependence of the absorption coefficient on electron density is reliably monotonic, in any event, when  $n_e > 10^{18} \text{ cm}^{-3}$ .

#### D. Conclusions

Of course, the range of temperatures within which accurate absorption measurements can be made will depend on the absorption length. However, we have found that neglecting free-free and bound-free absorption at high electron densities leads to large errors in the theoretical estimates of the relationship between absorption and temperature, viz., the serpentine trends shown in Figures 19 and 20 are missed. In addition, neglecting the effects of Doppler broadening leads incorrectly to the conclusion that





the absorption coefficient is insensitive to electron density.

Therefore, the earlier suggestion<sup>32</sup> that absorption be used to obtain temperature measurements rests on an inappropriately oversimplified theoretical approach. From our results, it seems that absorption of 4880 Å radiation by an argon plasma (once the temperature is determined independently) is more suited as an electron density diagnostic.

## VII. Summary

Tests for the existence and dynamic features of turbulent collisional shock fronts have not yet been performed. However, systematic trends in the performance parameters of pressure loaded arc driven shock tubes have been determined. The initial driver gas pressure is relatively unimportant. Adjusting the driver volume and the length of the discharge path can produce mixed results. Nonetheless, under the specified conditions, the Mach number increases with the cube root of capacitor energy without apparent limit. The relevance of fluorescence to ion density measurements in the ionizing shock wave has been confirmed. The absorption coefficient of an equilibrium argon plasma is computed, avoiding earlier restrictive assumptions, as a function of temperature and electron density. Our results suggest that the diagnostic applications of resonant absorption to temperature estimates are more difficult than previously expected.

When Tsuge's kinetic theory of turbulence is applied to flow with a simple nonequilibrium process, we find that the reaction rates for the turbulent and nonturbulent cases will be apparently different in direct proportion to the degree of chaos violation. Our studies of  $2\text{NO}_2 + \text{N}_2 \rightleftharpoons \text{N}_2\text{O}_4 + \text{N}_2$  in an adiabatically expanding shock tube's driver gas have revealed a systematic Reynolds number based association between pressure anomalies and distortions in the  $\text{NO}_2$  density history. We have analyzed these results using Tsuge's theory with its



boundary layer approximation. This approach seems to provide us with a nonempirical explanation of the well-known "hot spots" in turbulent nonequilibrium systems.

A boundary layer model allows us to determine characteristic scales and Reynolds numbers for a variety of turbulent shock tube discontinuities. With this model, Tsuge's kinetic theory for boundary layer flow with transition to turbulence becomes applicable. Minimum fluctuation levels as well as characteristic frequencies can be determined for unstable boundary layers with turbulent bursts. Previously published results on detonation waves have been successfully treated with these techniques. In addition, we find that our shock tube's driver gas flow produces fluctuations which can be successfully interpreted as turbulent bursts in contact surface flow. Therefore, our data and analyses support the approach to the theory of turbulence in Tsuge's works and, in particular, suggest a possible molecular interpretation for large coherent structures.

## References

1. Tsuge, S., Phys. of Fluids 17 (1974) 22.
2. Klimontovich, Y.L., The Statistical Theory of Nonequilibrium Processes (M.I.T. Press, Cambridge, Mass., 1967), p. 49.
3. Tsuge, S., Sagara, K., Physics of Fluids 19 (1976) 1478.
4. Landau, L.D. and Lifshitz, E.M., Fluid Mechanics, p. 116, Addison-Wesley Publ. Co., Reading, Mass., 1959.
5. Hall, J.G., J. Appl. Phys. 26, 698 (1955).
6. Istratov, A.G., Korovjanskaja, E.I., and Librovich, V.B., 12th Symposium (International) on Combustion, p. 779, Academic Press, New York, 1969.
7. Tsuge, S., Phys. Fluids 17, 22 (1974).
8. Osborne, M., S.I.A.M. J. Appl. Math. 15, 539 (1967).
9. Jordinson, R., J. Fluid Mech. 43, 801 (1970).
10. Tsuge, S. and Sagara, K., Phys. Fluids 19, 1478, (1976).
11. Johnson, J.A., III and Chen, S.C., Phys. Letts. 68A, 141 (1978).
12. White, D.R., Phys. Fluids 4, 465 (1961).
13. Lien, H. and Eckerman, J., A.I.A.A. J. 4, 1988 (1966).
14. Tsuge, S., Phys. Fluids, 17 22-23 (1974).
15. Tsuge, S. and Sagara, K., J. Stat. Phys., 12 403-25 (1975).
16. Tsuge, S. and Sagara, K., Phys. Fluids 19 1478-85 (1976).
17. Johnson, J.A., III and Chen, S.C., Phys. Letts. 68 141-3 (1978).
18. Landau, L. and Lifshitz, E., Fluid Mechanics (Reading, Mass.: Addison-Wesley) pp. 114-6 (1959).

19. Hall, J.G., J. Appl. Phys. 26 698-700 (1955).
20. Thompson, P.A., Compressible-Fluid Dynamics (New York: McGraw-Hill) pp. 374-442 (1972).
21. White, D.R., Phys. Fluids 4 465-80 (1961).
22. Bradley, J.N., Shock Waves in Chemistry and Physics (London: Methuen) pp. 135-47 (1962).
23. Zimet, E., J. Chem. Phys. 53 515 (1970).
24. Tennekes, H. and Lumley, J.L., A First Course in Turbulence (London: M.I.T. Press) pp. 210-1 (1972).
25. Dannenberg, R.E. and Silva, A.F., A.I.A.A. J. 10, 1563. (1972).
26. Dannenberg, R.E., A.I.A.A. J. 10, 1692 (1972).
27. Menard, W.A., A.I.A.A. J. 9, 2096 (1971).
28. Warren, W.R. and Harris, C.J., Aerospace Corporation Report (Sept., 1969) (Contract No. F04701-69-C-0066).
29. Dannenberg, R.E., Proceedings of the 11th International Symposium on Shock Tubes and Waves (1977). (To be published.)
30. Bradley, J.N., Shock Waves in Physics and Chemistry, Wiley Pub. Co. (1962).
31. Smy, P.R., Nature 193, 969 (1962).
32. Wheeler, C.B. and Troughton, J., Plasma Phys. 11, 391 (1969).
33. Lochte-Holtgreven, W., Plasma Diagnostics (North-Holland, Amsterdam, 1968) pp. 40-41, pp. 35-36.
34. Schnqpauff, R., Z. Astrophys. 68, 431 (1968).
35. Zel'dovich, Ya. B., and Raizer, Yu. P., Physics of Shock Waves and High Temperature Hydrodynamic Phenomena (Academic Press, New York, 1967) Vol. I, pp. 281-283.

36. Engelhardt, A.G., and Phelps, A.V., Phys. Rev. 133, A375 (1964).
37. See, for example, Yu. P. Raizer, Sov. Phys. Uspekhi 8, 650 (1966).
38. Schluter, D., Z. Phys. 210, 80 (1968).
39. Vorypaeva, N.S., Nikolaevskii, L.S. and Podomoshenskii, I.V., Opt. Spectrosc. (USSR) 44, 247 (1978).
40. Labat, J., Djenize, S., Cirkovic, Lj and Puric, J., J. Phys. B: Atom Molec. Phys. 7, 1174 (1974).
41. Griem, H., Plasma Spectroscopy (McGraw-Hill, New York, 1964) pp. 150-159.
42. Moore, C.E., Circular of the National Bureau of Standards 467 (U.S. Govt. Printing Office, Washington, D.C., 1949).

## APPENDIX A

BIBLIOGRAPHY: NSG 1314

- "Velocity Relaxation in Shock-Heated Fully Turbulent Gases",  
Bull. Am. Phys. Soc., 22, 1253 (1977). (J.A. Johnson,  
K. Oyedeki and S. Chen.)
- "Fluctuation Agglomerates in Transitional Flow", Bull. Am. Phys.  
Soc., 22, 1280 (1977). (J.A. Johnson)
- "Some Evidence of Reaction Distortion in Turbulent Nonequilibrium  
Flow", Bull. Am. Phys. Soc., 24, 75 (1979). (J.A. Johnson,  
R. Ramaiah and J. Santiago.)
- "A New Approach to Statistical Fluid Mechanics", Bull. Am. Phys.  
Soc., 24, 460 (1979). (J.A. Johnson)
- "Concerning a Molecular Basis for Understanding Transition to  
Turbulence in Gasdynamic Discontinuities", Bull. Am. Phys.  
Soc., 24, 460 (1979). (J.A. Johnson and Lin I.)
- "A Molecular Interpretation of Large Coherent Structures in  
Turbulent Flow", Bull. Am. Phys. Soc., (1979, to be published).  
(J.A. Johnson, R. Ramaiah and Y. Li).
- "Pressure Bursts and Product Enhancement in Fluctuating Reacting  
Flow", Bull. Am. Phys. Soc., (1979, to be published).  
(J.A. Johnson and R. Ramaiah)
- "Strong Shock Waves from a Low Capacity Discharge", Bull. Am.  
Phys. Soc., (1979, to be published). (J.A. Johnson, Lin I  
and J. Santiago)
- "The Absorption Coefficient of an Equilibrium Argon Plasma at 4880 Å"  
Bull. Am. Phys. Soc., (1979, to be published). (J.A. Johnson  
and J. Santiago)
- "Reaction Rate Distortion in Turbulent Flow", Phys. Letts., 68A,  
141 (1978). (J.A. Johnson and S.C. Chen)
- "Improving the Mach Number Capabilities of Arc Driven Shock Tubes",  
(Preprint, 1978, submitted for publication). (J.A. Johnson  
and J. Santiago)
- "Turbulent Bursts in a Shock Tube", (Preprint, 1979, submitted for  
publication). (J.A. Johnson)
- "Resonant Absorption in an Argon Plasma at Thermal Equilibrium",  
(Preprint, 1979, submitted for publication). (J.A. Johnson  
and J. Santiago)
- "Driver Gas Flow with Fluctuations", (Preprint, 1979, submitted for  
publication). (J.A. Johnson, W. Jones and J. Santiago)